Science Arts & Métiers (SAM)

is an open access repository that collects the work of Arts et Métiers Institute of Technology researchers and makes it freely available over the web where possible.

To cite this version :

A damaging beam-lattice model for quasi-brittle fracture

Margaux Sage[a,*], Jérémie Girardot[b], Jean-Benoît Kopp[b], Stéphane Morel[a]

[a]*University of Bordeaux, CNRS, Institute of Mechanical Engineering (I2M), Talence F-33400, France*
[b]*Arts et Metiers Institute of Technology, CNRS, Institute of Mechanical Engineering (I2M), Talence F-33400, France*

Abstract

This work aims to propose a new damaging beam-lattice model using the Discrete Element Method paradigm dedicated to the simulation of quasi-brittle fracture under complex loadings. Enrichment of the elastic Euler-Bernoulli beam link, inspired by the cohesive zone models, is proposed to provide a damageable behavior in mixed mode and contribution of frictional behavior is not considered in this first version of the damage model. The tensile contribution on the beam link is taken into account from the first order elongation of the beam while all other contributions, *i. e.* bending, shear, and torsion are considered from the second-order elongation of the beam. These orders of elongation refer to beam theory, where the first elongation is induced by a force normal to the cross-section and the second is the elongation of the curvilinear length of the beam resulting from shear, bending and torsion loads. As these two kinematics do not correspond to the conventional modes I, II, and III, a deep checking step of the model is undertaken. First, mixed-mode testing on a single beam is performed to monitor the energy components dissipated in each mode and to ensure that energy dissipated in mixed mode exhibits a monotonic evolution between boundary values related to pure modes. Based on this first verification, a tensile test and a compression one are simulated on a cylinder specimen to

*Corresponding author
  Email address:* `margaux.sage@u-bordeaux.fr` (Margaux Sage)

evaluate the model capabilities to qualitatively describe the well-known characteristics of quasi-brittle fracture such as failure facies, unilateral effect, and the ratio between the compression and tensile strength. Finally, the model is used to simulate a complex crack propagation test coming from the recent international *Carpiuc* benchmark.

1. Introduction

The modeling of quasi-brittle fracture has been widely studied. Of the many approaches considered, the finite element method is the most extensively used. The most popular finite element-based approaches are eXtended-Finite Element

5 Method (X-FEM), damage models, cohesive zone models, and more recently the phase-field model. Extended finite element method, developed in [1], [2],[3], simulates cracks within the finite element mesh using functions that enrich the degrees of freedom of the mesh nodes. This model performs well when simulating crack propagation for complex cracking paths. However, it struggles when

10 modeling processes such as fragmentation or multi-cracking, due to a large number of cracks present.

Another approach lies in damage models [4], [5], [6], [7]. They allow the stiffness of the material to be degraded locally in the meshes where cracks are present. Initially, faced with mesh dependency problems, work introducing regularisation

15 methods, such as non-local damage models [8] and gradient damage methods [9], made it possible to get rid of mesh dependency and snapback problems. Cohesive zone models are another approach that aims to model crack development zones ahead of cracks or defects [10], [11],[12]. This model is applied with the element method by adding cohesive elements between the meshes. Within these

20 elements placed ahead of the crack understudy, an adhesion force is defined that accounts for lower stresses ahead of cracks than those predicted by linear fracture mechanics. Different laws are used to define the forces of the cohesive

element. This model is particularly effective when studying a system with a crack that will propagate in a known direction. However, when the direction of

25 crack propagation is not known, a large number of cohesive elements must be used, with the result that the stiffness of the structure depends on the initial stiffness within the cohesive elements. More recently, work on the phase-field model [13], [14], [15], [16] has been carried out. This technique is based on the definition of a phase-field in the system. The presence of a crack is introduced

30 as the interaction between 2 phases. The separation of the material is allowed through the definition of the continuous phase field function which takes the values +1 and -1 on both sides of the crack. This model appears to be particularly effective in modeling phenomena such as branching and coalescence of cracks.

35 Although efficient in some cases, these models are confronted with the disadvantages of the finite element method, such as the mesh dependency and the high computational costs in the presence of a large number of cracks. The disadvantage of mesh dependence has been partially solved for the damage and phase-field models by introducing an internal length, the physical meaning of

40 which remains to be established. These difficulties in modeling fracture phenomena with the finite element method lead us to look at other numerical methods such as the discrete element method.

In general, a discrete disordered media is well known for its numerical ability to easily describe fracture mechanisms, and especially for elastic-brittle be-

45 haviors [17, 18]. The beam lattice approach in the Discrete Element Method paradigm is one of the various examples to simulate complex crack patterns [19].

The mainly used criterion for beam links consists in a cut-off method [20],[21],[22] in which the fracture of the beam is considered when a given threshold is reached. Among cut-off criteria, some are based on threshold stresses [19], strain thresh-

50 old defined from axial and rotational deformations [23] or using a cohesive model only in the longitudinal direction [24]. Improved cut-off criteria can also be used as in [25] where fracture only occurs if a stress threshold is maintained for a while to reach the fracture energy of the material. Similarly, many works, such

3

as [26], [27] or [28],[29] based on the rigid body spring model, use a cut-off cri-

terion on springs instead of beams to model the different phases composing the

concrete i.e. matrix, aggregate and matrix/aggregate interface. These numerical studies are mostly recent and emphasize the difficulty at the macroscopic scale to restore accurately fracture phenomenon under complex loadings where the fracture mechanisms need to be taken into account in mixed modes [30].

Moreover, a cut-off criterion takes place at the microscopic or mesoscopic scale and leads generally to very time-consuming simulations due to the need to describe the material (e.g. beam links) at the considered scale. In the goal to reduce simulation time, one solution consists of considering progressive damage of links instead of a simple cut-off criterion which leads implicitly to increase the scale associated with the links and consequently to reduce simulation time. Among the damaging link models, the one consisting of replacing a beam link by damaging springs (in normal and tangential directions) when the threshold is reached leads to various studies in the literature [31]. However, the analysis in [32] shows that beam links possess a better accuracy on fracture patterns than spring links. An improvement such as the development of a new criterion for beam links built on the spring link work would merely enhance the modeling of fracture behavior.

Indeed, most of the papers in the literature, such as detailed thereafter, define damage variable on the normal spring and the differences between the models come from the damage definition.

In [33], an equivalent deformation and principal stresses are evaluated. These quantities are deduced from mean strains and stresses in the normal and tangential directions expressed with normal and tangential forces and displacements.

On the other side of this mathematical approach, a simpler physical approach [34] is based on cohesive zone models where the linear slope damage law is set by cohesive energy in mode I, energy dissipated by the normal spring, and mixed maximum displacement. The normal and tangential stiffnesses are degraded by this damage. To take into account mixed-mode failure, a Mohr-Coulomb fracture criterion is defined from the mode I and mode II fracture energies.

4

⁸⁵ Another work inspired by cohesive zone models suggests giving an exponential evolution to the damage variable described thanks to displacement in the normal and shear directions [35]. A Mohr-Coulomb breakage criterion is also established.

The major drawbacks of this type of model are that they are only applied ⁹⁰ to normal and tangential forces respectively associated with the normal and tangential spring. The damage does not influence the moments. Moreover, these models are only satisfied when one of the failure modes (I or II) is predominant.

When a mixed-mode is present, *i. e. no mode of rupture is predominant*, the energy required for fracture exceeds those related to pure modes that is ⁹⁵ physically inconsistent.

Nevertheless, the results obtained with the different cohesive zone models applied on spring links lead us to focus on this approach of fracture.

A cohesive zone model is used to represent phenomena happening in the ¹⁰⁰ process zone. This consists in the simulation of a fictitious crack along with a cohesive interface for which a particular stress-displacement law is considered. This stress-displacement law consists generally of a first elastic regime up to the strength of the interface followed by a softening behavior describing the progressive damage of the stress and the stiffness leading to dissipated energy. ¹⁰⁵ The complete separation of the interface is obtained when the cohesive energy G_f is dissipated (area under the stress-displacement law). The initial works on cohesive zone were defined for pure mode fracture with the fictitious crack concept [36]. Moreover, different damage evolution laws can be used depending on the modeled material [37]. In the literature, four main types of laws seem to ¹¹⁰ emerge: a linear softening part [12], [38],a bi-linear softening slope [39], [11], [40], a tri-linear softening slope [41],[42] and an exponential softening [43],[44],[10] (This last softening is illustrated in the figure 1).
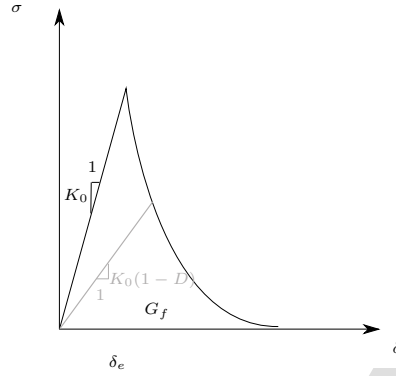
5

Figure 1: Stress-Displacement curve for a typical exponential damage law

It can be noticed that only three parameters are required to describe an exponential softening, the initial stiffness K_0, the maximum elastic displacement

115   δ^e, and the cohesive energy G_f.

For mixed loading such as tensile and shear loading, the use of a cohesive zone model for one of the three pure modes can be suitable only in the case of a preferential direction of crack propagation. In other cases, the need for a coupling between pure mode models is essential, in line with the wide range of

120   mixed-mode works carried out for example in [45],[46] [47]. Indeed, an uncoupled model would lead to dissipated energy peak for mixed-mode rupture, *i.e.* more energy would be necessary for rupture happening than in pure modes, which is non-physical. In terms of energy, a coupled model ensures that energy dissipated for fracture in mixed mode is bounded by energies corresponding to pure modes

125   and that energy tends to mode I energy (respectively mode II energy) when mixed-mode fracture tends to pure mode I fracture (resp. mode II). Such a model is usually defined from pure modes. A parameter β monitoring mixed-mode rate is expressed from displacements related to mode I and mode II such as $\beta = \frac{\delta_{II}}{\delta_I}$.

130   From this parameter and the ones provided by pure mode laws, the mixed-mode damage evolution law is updated at every step of the simulation.

This cohesive zone model provides a useful approximation of fracture processes of materials and its installation at a mesoscopic scale allows reducing simulation time. Moreover, its ability to taking into account mixed mode at
135 fracture appears as a powerful model applicable to the Discrete Element Method (DEM). However, if the use of damaging link model through degraded spring is the subject of many works today, the solution consisting in using damage model in beam link is much less studied whereas DEM based on beam links is known to describe crack paths with better accuracy compared to those obtained from
140 spring links [32].

The present work is inspired by the ones in [48, 49] which propose damageable beam-lattice domain in 2D.

Here, an original damage model acting on tridimensional beam-lattice domain is proposed. Its capabilities to describe the general aspects of the quasi-
145 brittle fracture and in particular the cracking paths are shown and discussed. Nevertheless, in this first version of the model, the frictional aspects of the quasi-brittle failure are not taken into account. Hence, the model will fail to describe the values of the residual displacements observed from an unloading following
150 a damage in traction for example, [50], [51]. Nevertheless, if the capacities of a discrete element model to naturally describe the friction between particles are not exploited in this first version of the model(usually, a classical Hertz-Mindlin model is implemented for the broken particles that are in contact like in [52]), the contact between discrete elements is used in order to describe the unilat-
155 eral effect of quasi-brittle materials and the capacities of the model to describe quasi-brittle mixed mode I+II cracking is studied. In addition, the definition of a cohesive zone model at the virtual Voronoi interface shared by two neighboring discrete elements makes it possible to get rid of the problems of initializing the stiffness of the cohesive element observed with the finite element method.
160 Indeed, the stiffness of the beams connecting the discrete elements is naturally used for this purpose. Moreover, the introduction of this cohesive behavior, via a damage variable within the Euler-Bernoulli beams of the lattice, provides an

7

energetic control of the softening phase of the failure. The damage model is implemented within an Euler-Bernoulli beam-lattice rather than a Timoshenko

165 one because if Timoshenko beams provide a more accurate description of the contribution of shear, they would lead to new parameters to be calibrated. Their use would then require the development of a new calibration process. The reliability of the elastic calibration process for Euler-Bernoulli beams led us to choose these beams for our model.

170 The model of the damaging beam and the closure management method are detailed in the first part of this paper. Then, three main classical mechanical tests are carried out. As the last section of the paper is related to experimental comparisons, the authors analyze the results of these preliminary simulation tests to evaluate only the qualitative response to the model related to the cali-

175 bration of the damage parameters. Typical failure mechanisms for quasi-brittle materials are observed such as the unilateral effect or the ratio between compressing and tensile strengths. Tensile and compressive tests under monotonic and cycling loading are performed in this sense. Finally, to compare the model with experimental results, two tests from the recent *Carpiuc* benchmark pro-

180 posed in the two previous ECCOMAS International Conferences on Computational Modeling of Fracture and Failure of Materials and Structure (CFRAC) [53] are simulated. They consist of a mixed loading including tensile and shear forces as well as a bending moment applied to pre-cut specimens (single- and double-notched).

185 **2. The Damaging Beam Model (DBM)**

2.1. Beam lattice domain

Contrary to the finite element method, the continuum mechanics are not applicable for the discrete element method. Indeed, the principle of the discrete element method consists of discretizing a continuous media with particles. The

190 discrete element method, created for granular materials, is based on the interactions between the particles. These interactions consist of forces and moments

8

applied on the discrete elements. In the case of cohesive media, the interactions between discrete elements are represented thanks to beam links. The forces and moments induced by the beam on the elements are defined from the theory of ₁₉₅ beams. Thus, for each beam, three forces, one normal and two tangential forces are calculated. Likewise, three moments, one torsion, and two bending moments are determined. These forces and moments and the induced kinematics for an Euler-Bernoulli beam can be found in the work of André *et al.* in [19].

₂₀₀ These forces and torques are applied on each discrete element attached to the beam. These elements can be of different shapes, such as spherical or polygonal shapes and may or may not be in contact with each other. Thereafter, two examples of discretization are shown in figure 2. The first one consists in spherical discrete elements which are not in contact while in the second one, ₂₀₅ polygonal discrete elements in contact are represented. In both cases, each discrete element is connected to its neighbors thanks to links as beams.

(a) Discretization with Spherical discrete elements linked by beams

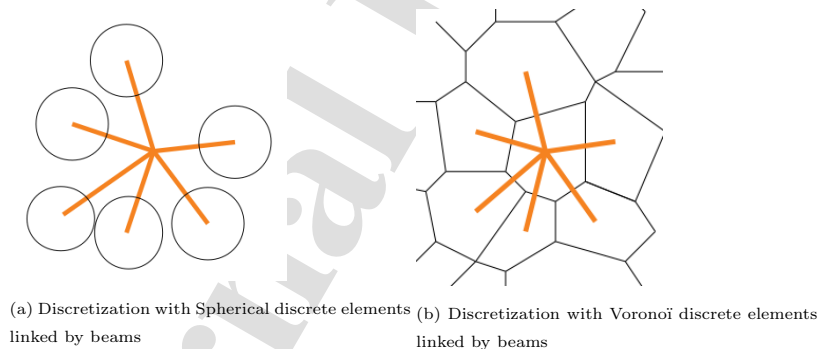(b) Discretization with Voronoï discrete elements linked by beams

Figure 2: Examples of discretization

However, note that the use of discrete element of polygonal shape makes difficult the contact detection between discrete elements compared to the case of spherical discrete elements. Neither the discrete elements are spherical or ₂₁₀ polygonal and in contact or not, the volume of material associated with each discrete element can be obtained from a Voronoi tessellation as shown in figure

9

3. From this point of view, the common material area between two neighboring discrete elements, $A_{Voronoi}$ as shown in figure 3, can be associated with the beam linking both discrete elements. Note that the surface $A_{Voronoi}$ is perpendicular

215 to the axis of the beam link and that the classical kinematic fracture modes between two neighboring Voronoi volume of material can be considered from the surface $A_{Voronoi}$.
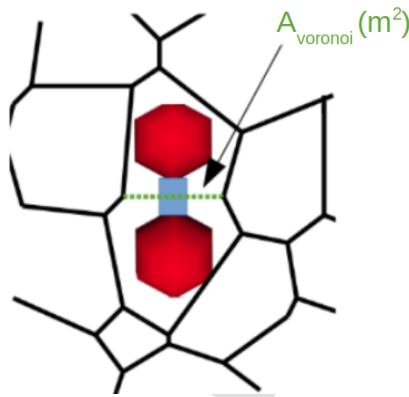

Figure 3: Scheme of material volumes associated to spherical discrete elements

This three-dimensional beam model is implemented in the discrete element workbench *GranOO* [54]. As for any discrete element method code, the al-

220 gorithm assesses first forces and torques on each discrete element. With the Newton law, accelerations are deduced. Thanks to an integration scheme, velocities and displacements are calculated from accelerations. In GranOO, an explicit scheme is used, the Verlet Velocity scheme [19]. To ensure stability and convergence, a critical time step Δt_{crit} is determined and the calculation time

225 step Δt is taken with a ratio of ten percent *i. e.* $\Delta t = 0.1 \Delta t_{crit}$.

The Damaging Beam Model (DBM) detailed thereafter consists in an improvement of this beam model inspired by cohesive zone models.

10

2.2. Mixed mode cohesive model

The damaging beam model consists of the definition of a damage variable D
for each beam. The beam Young modulus is thus degraded inducing a decrease
in forces and torques :

$$E = (1 - D)E_0, \tag{1}$$

where E_0 and E correspond to the initial and current Young modulus. The
evolution law of D is inspired from the mixed-mode cohesive zone model found
in [47], and in this work, all the three classical crack opening modes, I, II, and
III are used to explicit the evolution of the damage.

The activation of the damage evolution is governed by a mixed initiation
criterion expressed as :

$$\sum_{k=\text{I,II,III}} \left(\frac{\delta_k}{\delta_{e,k}} \right)^2 = 1, \tag{2}$$

where δ_k is the current displacement for the mode k and $\delta_{e,k}$ is the elastic limit
also for each mode.

Assuming an exponential shape of the softening as shown in figure 1 for all
modes, the evolution of the damage variable can then be written as:

$$D = 1 - \frac{\widetilde{\delta_e}}{\widetilde{\delta}} \exp \left(\frac{2\widetilde{K}}{2\dfrac{\widetilde{G_f}}{\widetilde{\delta_e}} - \widetilde{K}\widetilde{\delta_e}} (\widetilde{\delta_e} - \widetilde{\delta}) \right), \tag{3}$$

where $\widetilde{K}$, $\widetilde{\delta_e}$ and $\widetilde{G_f}$ are the cohesive law parameters in the mixed space (*i.e.* a
combination of cohesive parameters for each crack opening modes I, II, III. $\widetilde{\delta}$ is
the current displacement also projected in the mixed space. The projection in
the mixed space will be described in the section 2.3.2.

Finally, a cut-off criterion is used to make the fracture of the beam effective
when D tends to 1. It is assumed that total fracture, *i.e.* the beam is deleted,
happens when the mixed stress in the beam reaches one percent of the mixed

11

peak stress after the damage activation. In the DBM, the criterion is translated
into an ultimate displacement $\widetilde{\delta_u}$:

$$\widetilde{\delta_u} = \widetilde{\delta_e} - \left(\frac{2\dfrac{\widetilde{G_f}}{\widetilde{\delta_e}} - \widetilde{K}\widetilde{\delta_e}}{2\widetilde{K}} \right) \ln\left(\frac{1}{100} \right). \tag{4}$$

2.3. Definition of the pseudo modes

2.3.1. Kinematic equivalences

The damage evolution law and the damage initiation criterion depend on four
variables $\widetilde{\delta}$, $\widetilde{\delta_e}$, $\widetilde{K}$ and $\widetilde{G_f}$ that need to be evaluated at each iterations. These
mixed law variables are defined from the variables of the three cohesive laws for
each pure mode. As these modes are connected to a specific opening kinematic
that is not similar to a Bernoulli beam one, it is then required to propose an
equivalence. The representation of the pure mode fractures is displayed in the
table 1 as well as their assumed equivalences for the beam with respect to the
surface $A_{Voronoi}$ (Figure 3). From these beam kinematics, a cohesive law is
defined for each of the pure modes. To determine a cohesive law, only three
parameters are needed: a stiffness K, a maximum elastic displacement δ_e and
a cohesive energy G_f. Note that cohesive laws relate stress to displacement,
therefore the stiffness K must be in [N/m] and the displacement δ in [m].

Tension. First, the equivalence of mode I of failure appears obviously as a result
of the tensile effect. Thus, the displacement describing this mode of failure is
the elongation of the beam. The stiffness defined for this mode corresponds to
the tensile stiffness of the beam. Their respective expressions are given by:

$$\begin{cases} \delta_{tension} & = & L - L_0 \\ \\ K_{tension} & = & \frac{E_0}{L_0} \end{cases} \tag{5}$$

12

Shear and bending. The definition of mode II becomes less straightforward because of the two contributions, shear, and bending. Indeed, defining a displacement and a stiffness providing monitoring of shear contributions F_y and F_z as well as bending contributions T_y and T_z is more complicated. Nevertheless, it can be highlighted that both shear and bending loads induce an increase in beam length. Hence, the difference between the curvilinear length of the beam and the beam length obtained only by tensile loading could be a displacement monitoring shear and bending effects. The mode II stiffness is then determined by averaging these two stiffnesses. For Mode II stiffness, the shear and bending stiffnesses can be written as:

$$
\begin{cases}
\delta_{shear/bending} & = \quad L_{curve} - L \\[2ex]
K_{shear} & = \quad \dfrac{E_0 I_g}{L_0^2 R_{beam}} \\[2ex]
K_{bending} & = \quad \dfrac{E_0}{L_0}
\end{cases}
\tag{6}
$$

Torsion. For mode III failure, the parameters of the cohesive law are derived from torsional effects. Thus, the displacement is naturally expressed as that induced by the torsion angle. The mode III stiffness is also assigned the torsional stiffness. These displacement and stiffness are expressed as:

$$
\begin{cases}
\delta_{torsion} & = \quad R_{beam}\theta_{torsion} \\[2ex]
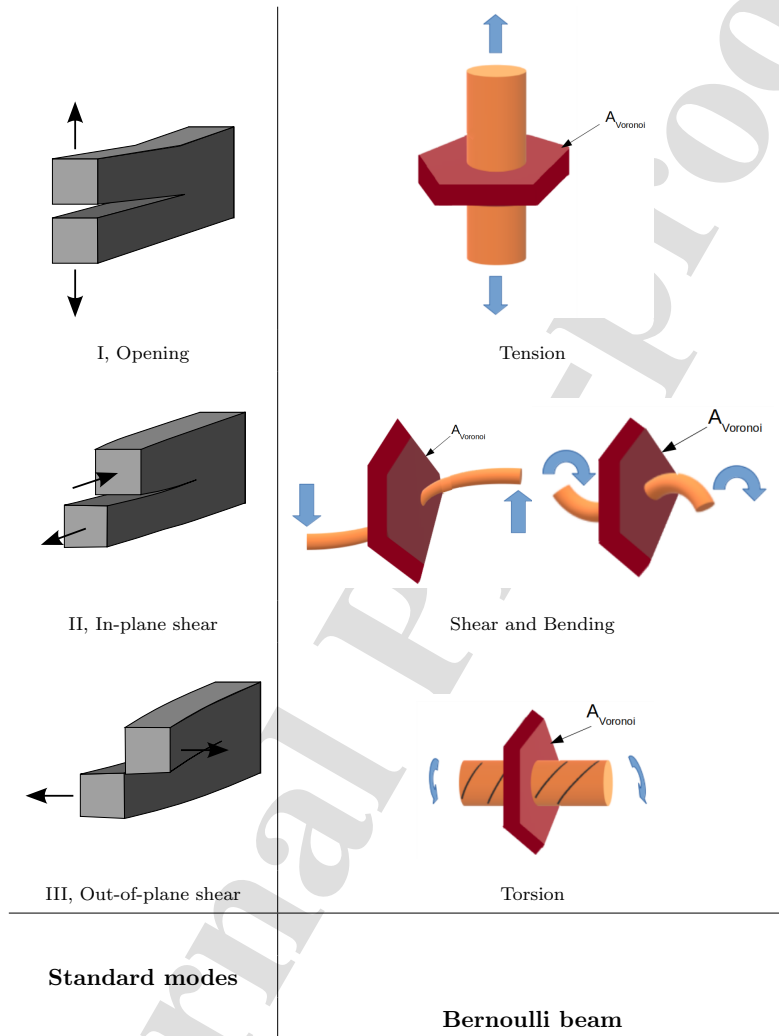K_{torsion} & = \quad \dfrac{E_0}{(1+\nu)L_0}
\end{cases}
\tag{7}
$$

13

Table 1: Conventional modes of fractures and the equivalent modes for a beam with respect to the surface $A_{Voronoi}$

2.3.2. Pseudo modes definition

270   Three pseudo pure modes of fracture applied to the beam equivalent to the conventional modes of fracture are defined. However, a mixed-mode combining

14

three pure modes would be unnecessarily complicated. Indeed, as explained in the paper [55], when the beam is deformed, the energy is principally composed of tension energy. In this way, tension effects can be considered as the major

275 mode of fracture of the mixed-mode model and will be named as pseudo mode I noted as mode I* . On the other hand, contributions from torsion loads are low and torsion and bending fractures appear on the same surface as shown on kinematic schemes in the table 1. Thus, a single pseudo mode II can be defined from both torsion and bending effects. More generally, all loading on the beam

280 different from tension loading is considered belonging to pseudo mode II noted as mode II*.

Moreover, the low contributions of bending and torsion loads ensure that the mode II* will not be predominant and thus, that the assumption of combin-

285 ing torsion and bending effects is suitable. By an energy analysis, the pseudo mode II (mode II*) can be considered as an energy E_{II^*}, the sum of energies of mode II E_{II} and mode III E_{III} of fracture which will be dissipated when the surface shared by Modes II and III is fractured. This new energy can be as well expressed as a function of a stiffness K_{II^*} and a displacement δ_{II^*}.

290

Consequently, two pseudo pure modes, mode I* and mode II* are defined from the equivalences of the 3 conventional pure modes detailed in the previous paragraph. Mode I* is similar to mode I, and corresponds to first order elongation of the beam. Thus, fracture parameters of the pseudo mode I (mode I^*)

15

can be expressed as :

$$
\begin{cases}
\delta_{\mathrm{I}^*} & = & L - L_0 \\[2ex]
K_{\mathrm{I}^*} & = & \dfrac{E_0}{L_0} \\[2ex]
\delta_{e,\mathrm{I}^*} & = & \varepsilon_{e,\mathrm{I}} L_0 \\[2ex]
G_{f,\mathrm{I}^*} & = & \dfrac{A_{beam}}{A_{voronoï}} G_{f,\mathrm{I}}
\end{cases}
\tag{8}
$$

Concerning the cohesive energy for mode I*, the choice is made to introduce directly the energy extracted from experimental tests in mode I failure. Similarly, the maximum elastic displacement in mode I* is deduced from experimental maximum elastic strain noted $\varepsilon_{e,\mathrm{I}}$. However, the lattice character of the method implies a resetting step of the cohesive energy. In the aim of avoiding another calibration step, the beam parameters are directly calculated from the material ones. However, it should be noted that energy conservation is not valid here. Indeed, the elastic calibration of the Young modulus induces a rigidity of the beam which is greater than the rigidity of the material. Thus, in the case of energy conservation, the beam fracture energy would be lower than the elastic energy accumulated in the beam, which is not physically allowed. Hence, to estimate the fracture energy of the beam, it is assumed that the ratio of the fracture energy of the beam over the cross-section area of the beam is equal to the ratio of the fracture energy of the material over the surface area $A_{Voronoi}$.

The area $A_{Voronoi}$ is the material surface modeled as defined in Section 2.1 and obtained from voronoï mesh. The energy release rate of each beam is set as shown in equation (8).

Mode II* represents the second-order of elongation of the beam. The pa-

16

310 rameters of the pseudo mode II (mode II^*) are written as :

$$
\begin{cases}
\delta_{\mathrm{II}^*} & = \; L_{curve} - L + R_{beam}\theta_{torsion} \\[2ex]
K_{\mathrm{II}^*} & = \; f_{shear}K_{shear} + f_{bending}K_{bending} + f_{torsion}K_{torsion} \\[2ex]
\delta_{e,\mathrm{II}^*} & = \; \alpha\delta_{e,\mathrm{I}^*} \\[2ex]
G_{f,\mathrm{II}^*} & = \; \alpha G_{f,\mathrm{I}^*}
\end{cases}
\tag{9}
$$

The mode II^* displacement is expressed as the sum of the mode II and mode III displacements. To express a mode II^* stiffness, a weighted average is obtained from the shear, bending, and torsion stiffnesses. The weights used to calculate the Mode II^* stiffness are given by :

$$
\begin{cases}
f_{shear} & = \; \dfrac{F_y + F_z}{F_y + F_z + \dfrac{T_y}{L} + \dfrac{T_z}{L}} \dfrac{\delta_{shear/bending}}{\delta_{\mathrm{II}^*}} \\[4ex]
f_{bending} & = \; \dfrac{\dfrac{T_y}{L} + \dfrac{T_z}{L}}{F_y + F_z + \dfrac{T_y}{L} + \dfrac{T_z}{L}} \dfrac{\delta_{shear/bending}}{\delta_{\mathrm{II}^*}} \\[4ex]
f_{torsion} & = \; \dfrac{\delta_{torsion}}{\delta_{\mathrm{II}^*}}
\end{cases}
\tag{10}
$$

315 where f_{shear}, $f_{bending}$ and $f_{torsion}$ correspond to the weight of the shear, bending, and torsion stiffnesses in the estimation of the related to the pseudo mode II. Note that these weights are functions of the shear forces F_y and F_z and the bending torques T_y and T_z from the theory of beams.

320 Since the mode II^* energy has no physical equivalent, the choice is made to express this energy in proportion to the mode I^* cohesive energy. For this pur-

17

pose, an α parameter is introduced and monitors the mixed-mode contribution and will need to be calibrated.

In summary, only one parameter needs a calibration step, the other parameters are set from experimental data.

Based on the pseudo pure modes previously defined, the parameters corresponding to a "pseudo" mixed-mode are expressed according to [56] and [47] such as:

$$
\begin{cases}
\widetilde{\delta} &= \delta_{I^*}\delta_{II^*}\sqrt{\dfrac{1+\beta^2}{\delta_{II^*}^2+\beta^2\delta_{I^*}^2}} \\[3mm]
\widetilde{K} &= \sqrt{\dfrac{K_{I^*}^2+\beta^2 K_{II^*}^2}{1+\beta^2}} \\[3mm]
\widetilde{\delta_e} &= \delta_{e,I^*}\delta_{e,II^*}\sqrt{\dfrac{1+\beta^2}{\delta_{e,II^*}^2+\beta^2\delta_{e,I^*}^2}} \\[3mm]
\widetilde{G_f} &= \dfrac{\delta_{e,II^*}^2}{\delta_{e,II^*}^2+\beta^2\delta_{e,I^*}^2}G_{f,I^*}+\dfrac{\beta^2\delta_{e,I^*}^2}{\delta_{e,II^*}^2+\beta^2\delta_{e,I^*}^2}G_{f,II^*} \\[3mm]
&= \widetilde{G_{f,I^*}}+\widetilde{G_{f,II^*}}
\end{cases}, \qquad (11)
$$

where β corresponds to the pseudo mixed mode ratio with :

$$\beta = \frac{\delta_{II^*}}{\delta_{I^*}} \qquad (12)$$

The mixed mode stiffness $\widetilde{K}$, the maximum elastic displacement of the mixed mode $\widetilde{\delta_e}$ and the mixed mode cohesive energy $\widetilde{G_f}$ are functions of β. The last term $\widetilde{G_f}$ can be written as a combination of two contributions of both pseudo mixed modes $\widetilde{G_{f,I^*}}$ and $\widetilde{G_{f,II^*}}$. These decomposition will be used especially in section 2.6 for validation.

18

335   The four terms in equation 11 are used to feed the initation and evolution criterion defined previously in equations (2) and (3). At every step of the simulation, a different damage law is defined. Indeed, between two incremental times, displacements δ_{I*} and δ_{II*} evolve with the fluctuation of loads applied to the structure. An update of parameter β value is required, modifying all

340 parameters from the damage evolution law. In this way, for a zero β value, the pure mode I* law is restored while for an infinity β value, the mode II* law is found.

2.4. Closure model

    A quasi-brittle material submitted to a tension loading exhibits a decrease

345 of its stiffness in the tension direction due to the development of micro-cracks oriented preferentially in the normal direction to one of the tension loadings. Nevertheless, if this damaged material is then submitted to a compression loading applied in the direction of the preceding tension loading, the material exhibits a restoration of its initial stiffness due to the closure of micro-cracks. To

350 reproduce this phenomenon called as the unilateral effect, closing forces and torques are added. Thus, the sum of the forces and torques in the re-closed link is equal to the forces and torques of an undamaged beam loaded in compression, *i.e.* such that :

$$\left\{ \begin{array}{c} \vec{F} \\ \vec{T} \end{array} \right\} = \left\{ \begin{array}{c} \vec{F}_{Damagebeam} \\ \vec{T}_{Damagebeam} \end{array} \right\} + \left\{ \begin{array}{c} \vec{F}_{closure} \\ \vec{T}_{closure} \end{array} \right\} \tag{13}$$

    In addition, micro-crack reclosure occurs within the entire representative ele-

355 mentary volume (REV) modeled by the reclosed beam. It is therefore necessary to take into account the part of the REV represented by void. Thus, during the reclosure of two discrete elements, the forces $F_{closure}$ are transmitted along a surface that does not correspond to the surface of the beam but to the Voronoi surface common to both elements, illustrated in figure 3. The stiffness related

19

360 to the reclosure force $F_{closure}$ can be expressed as :

$$K_{closure} = D \frac{E_0 A_{vorono\ddot{i}}}{L_0} \qquad (14)$$

Note that the natural capacity of DEM to detect contact between discrete elements is used in order to activate closure forces (see equation 13). Nevertheless, if contact detection is activated, the frictional behavior between discrete elements is not considered in order to evaluate the capacities of the alone damage
365 beam model to describe quasi-brittle failure.

2.5. Sequential Algorithm

The process carried out at each time step for each beam is detailed in figure 4 and includes the application of the damage model as well as the closure model.
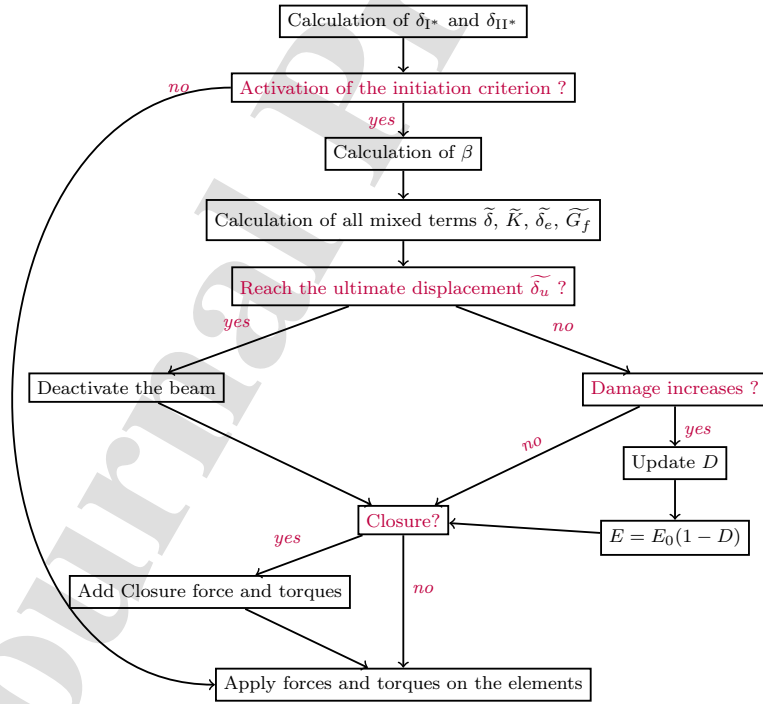
Figure 4: Sequences for the application of the damage model and closure for each beams.

20

2.6. Mixed mode Test on a single beam

370 Physically, the mixed-mode fracture energy of the beam has to be bounded by the pure mode fracture energies. For various materials, the most energetic mode (i.e. the mode exhibiting the larger cohesive energy) corresponds to pseudo mode II while the least energetic corresponds to pseudo mode I. Thus, mixed-mode should require cohesive energy ranged between those of pure modes,

375 and the evolution of this one with respect to the mixed-mode indicator β should be monotonic. As our model is based on energy driving, it appears essential to verify this energy trend.

The non-common mode definition used in the model leads us to take precautions and to achieve a deeper checking phase. For this purpose, a test is carried

380 out on a single beam loaded with a mixed tensile-torsion boundary condition to simulate various mixed-mode cases.

Thus, a displacement in the longitudinal direction is imposed at a beam end. The other end is subjected to a torsion rotation around the beam axis. With such a loading, pseudo mode I displacement is provided by longitudinal

385 displacement while pseudo mode II displacement is induced by torsion angle. Hence, the different pseudo mixed mode ratio (β) values are generated in the beam with the variations of the displacement and rotation imposed at the beam ends. When β is equal to 0, a pure tension loading is applied, then is increasing with the rotation value on the beam.

390 The input parameters for the damage law are given in the table 2.

$G_{f,\mathrm{I}}$	$60 \ J.m^{-2}$
$\varepsilon_{e,\mathrm{I}}$	10^{-4}
α	5

Table 2: Damage law parameters for the validation tests on a single beam.

The evolution of the mixed-mode fracture energy as a function of the mixed-mode indicator β is plotted in the figure 5. The mixed-mode fracture energy ($\widetilde{G_f}$) of the beam corresponds to the sum of the components of mode I* ($\widetilde{G_{f,\mathrm{I}^*}}$)

21

and of mode II* ($\widetilde{G_{f,\text{II}^*}}$) of the energy and here can be either tensile energy or
torsion energy. Thus, both mode I* and mode II* energy components are drawn.
It can be noted that each component (pseudo mode I energy or pseudo mode
II energy) is lower than the corresponding pure mode energy value. Then, the
mixed-mode fracture energy is bounded by pure mode I* fracture energy and
mode II* fracture energy. Moreover, it can be observed that when β tends
towards 0, the mixed-mode fracture energy tends to the one expected from
pure mode I* as well as its tensile component. Similarly, for a high value of
β parameter, the mixed-mode fracture energy reaches the one associated with
mode II*.
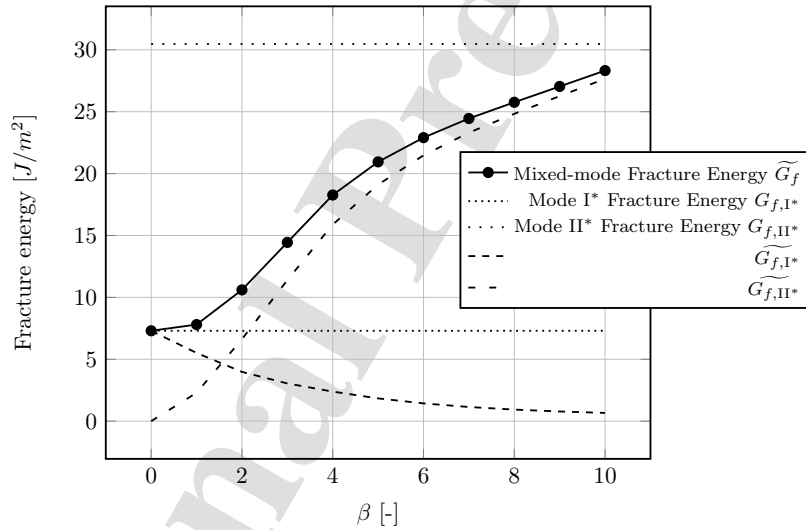
Figure 5: Fracture Energies as function of the pseudo mixed mode ratio β on a single beam.

The analysis of the energy dissipated shows that the proposed damage model
is consistent in terms of energy.

22

3. Calibration and qualitative response of the model

3.1. Material

The model developed here, is built to be suitable for any quasi-brittle material simulation. Among quasi-brittle materials, concrete is subject of numerous

410 studies available in literature [57],[58], [59],[60],[61],[62] and is chosen here in order to test the model in various fracture modes. Indeed, the main characteristics of the concrete failure under compressive and tensile loading are well-known and are here simulated to evaluate the relevance of the damage cohesive beam model. The simulated responses in tension and compression will be simply qualitatively

415 compared to the experimental ones while the ratio of compression and tensile strengths obtained from simulation will provide a quantitative comparison with respect to the well-known ratio of 10 expected for quasi-brittle materials.

Prior to simulating tests, according to [55], a calibration step is realized to determine the model parameters allowing to simulate concrete elastic behavior.

420 The elastic parameter values for macroscopic and model scales are displayed in the table 3.

Macro scale	Model scale
$E_M = 39.4 GPa$	$E_\mu = 189.5 GPa$
$\nu_M = 0.2$	$\nu_\mu = 0.3$
	$r_\mu = 0.6$

Table 3: Model and macroscopic elastic parameters for concrete, where r_μ is the radius ratio i. e. the ratio between each beam radius and the average radius of its linked discrete elements.

3.2. Tensile Test on a cylindrical specimen

A tensile test is performed on a cylindrical specimen. The dimensions of the specimen are 70 mm for the length and 35 mm for the radius as indicated in
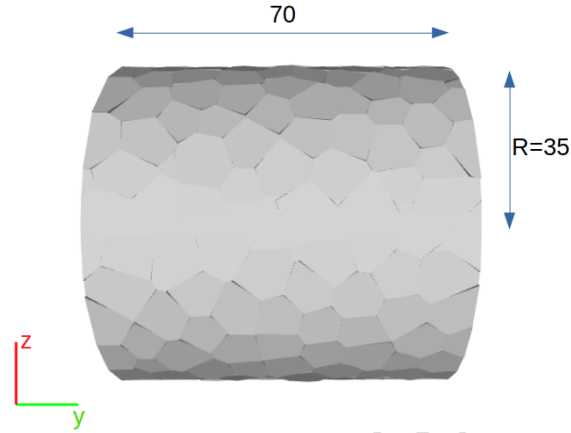
425 figure 6.

23

Figure 6: Voronoi mesh of the cylindrical specimen (values in mm)

In order to simulate a concrete-like material, the fracture energy $G_{f,\mathrm{I}}$ is fixed arbitrarily to the value of $G_{f,\mathrm{I}} = 50 J/m^2$. Then, the model fracture energy of each beam is estimated according to the relationship $G_{f,\mathrm{I}^*} = \frac{A_{beam} G_{f,\mathrm{I}}}{A_{voronoï}}$ as previously mentioned. The elastic strain $\varepsilon_{e,\mathrm{I}}$ is fixed to the value 8×10^{-5} in order to simulate a tensile strength of the specimen equal to $f_t = 4 MPa$. Finally, the value for α is given arbitrarily at 8.

To remain in a quasi-static regime, the displacements imposed on the end cross-sections are such that a speed of 1.6 mm/s is ensured. The response stress-strain obtained from the simulation is plotted in figure 7.

24
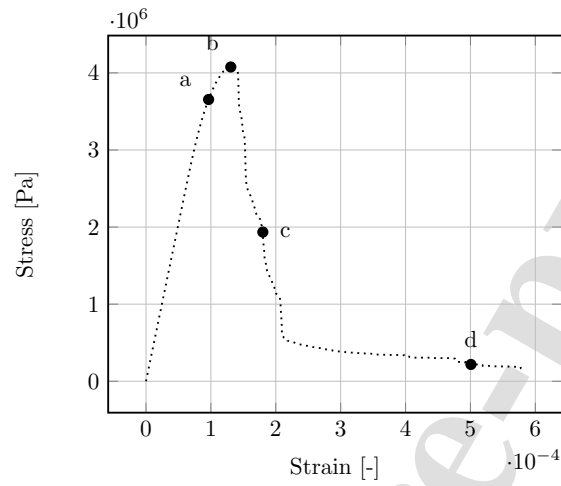
Figure 7: Stress-Strain response obtained from the DBM for a tensile test on a cylindrical specimen

[435] The trend displayed in the figure 7 corresponds to the expected quasi-brittle behavior. Indeed, peak stress of 4.1 MPa is obtained which is consistent with the experimental values observed for this material [63],[64], [65]. Furthermore, the sharp softening occurring after the peak stress is characteristic of the brittle character of fracture expected from a non-stabilized tensile loading.
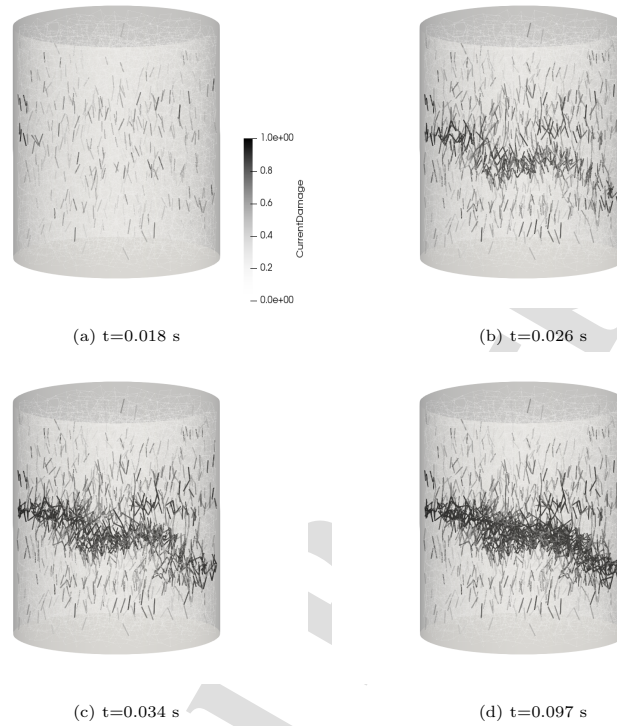
25

(a) t=0.018 s

(b) t=0.026 s

(c) t=0.034 s

(d) t=0.097 s

Figure 8: Evolution of damage fields during a tensile test

The damage fields, corresponding to 4 different times of the simulations (represented by the points a,b,c and d in figure 7), are plotted in figure 8. After a first step in which the damage is diffuse in the specimen, a localization of damage in a plane approximately horizontal (i. e. a plane perpendicular to the tensile direction) is observed (b) then the fracture process continues through a damage percolation process near this plane up to the complete failure of the specimen.

The localization of the damage occurs randomly at the height of the cylinder. Every beam of the network is allowed to damage, no artifices need to be added to obtain the localization.

26

450

The repeatability of this test on different initial beam networks is shown in figure 9 and allows to verify that the crack is randomly located in the cylinder but always around a horizontal plane.
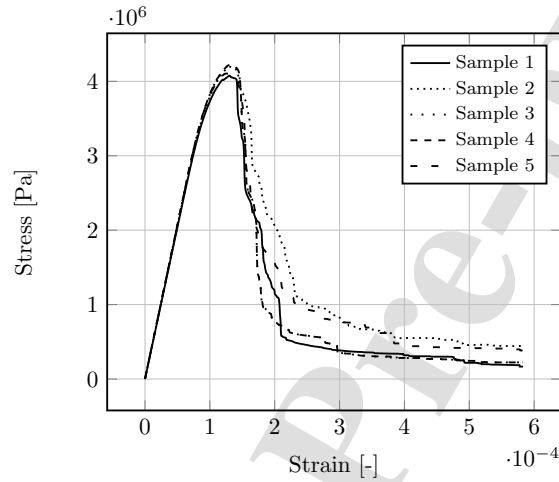

Figure 9: Stress-strain response for five samples of different initial distribution under a tension loading.

The stress-strain responses for five different samples composed of 5700 dis-
455 crete elements are depicted in the figure 9. The variability of the lattices does not influence the stress peak. The softening is slightly affected by the initial beam distribution chosen. The energy release rates of the specimens are calculated from the area under the stress-displacement curves divided by the cross-section area of the sample and reported in the table 4. The average energy release rate is
460 48.8 J/m^2. Consequently, the energy release rate obtained with the simulations tends to the energy release rate 50 J/m^2 input in our model. The method of calibration of the cohesive energy proposed in this paper is therefore validated.

27

Sample n	$G_{f,\mathrm{I}}$ (J/m^2)
1	43.8
2	57.4
3	46.4
4	44.09
5	52.7

Table 4: Macroscopic Energy dissipated by the different samples

Finally, the influence of the number of discrete elements on the stress-strain response is studied, to quantify the number of elements ensuring a qualitative result. This convergence study is undertaken thereafter, from a sample constituted by a number of discrete elements ranged between 1 700 and 22 000 as shown in figure 10.

For any element numbers, the expected stress-strain shape is exhibited and the brittle tendency is recovered even for a coarser specimen. However, for the sake of accuracy, a minimum of 5700 elements is suitable to provide a deviation under 10 % of finer mesh peak stress and energy. In other words, an elastically accurate specimen will display precisely the damaging behavior.
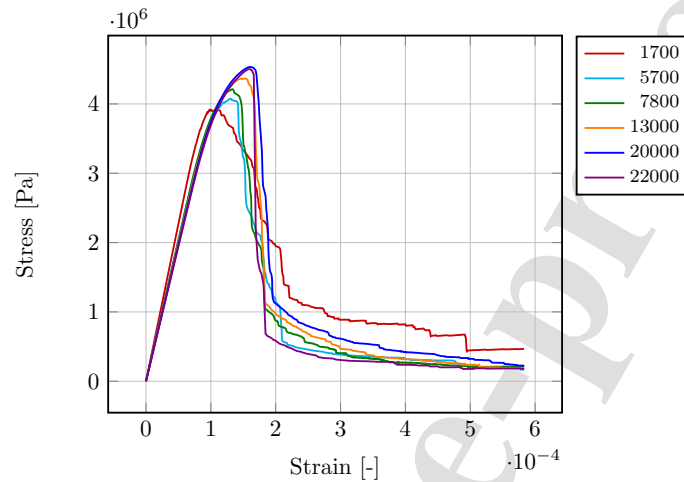
Figure 10: Study of the convergence on a cylinder under tension for an increasing number of elements.

The convergence of the model has been studied thanks to two indicators, fracture energy, and peak stress. The convergence for each factor is illustrated in figure 11. To ensure the validity of the convergence study, the variability of the results is taking into account by reproducing the tests on a minimum of 5 specimens for each discrete element number. The stress-strain curves plotted in figure 10 correspond to the average of the responses obtained from 5 specimens. On the left side, it can be noted that the fracture energy converges rapidly. Indeed, even for a coarse specimen, the average error on the fracture energy obtained is close to zero. The case of a large error on the fracture energy is induced by the various initial beam networks available. For the finer specimens, this effect is noticeable. In addition, the impact of the variability of initial networks seems to become constant for specimens composed of more than 13000 discrete elements. This minimum influence of the variability can be quantified as approximately 10%.

If the convergence of the energy is reached from 13 000 discrete elements, the convergence of the peak stress seems to require the use of 20 000 discrete

29

elements to be reached, as shown in figure 11b. Nevertheless, the shape of the
490   stress-strain responses becomes acceptable from 5 700 discrete elements in so far
as all responses exhibit a post-peak consistent with the one expected in tension
for a quasi-brittle material, *i. e.* marked from a first sudden decrease of the
stress followed by a softening tail. As a consequence, for the peak stress as well
as the fracture energy, the values obtained for the 5700 discrete elements remain
495   fairly accurate with an error of 7.3% and 3% respectively. In such a case, the
tests on a 5700 sample are privileged.

(a) Energy convergence

(b) Peak Stress convergence
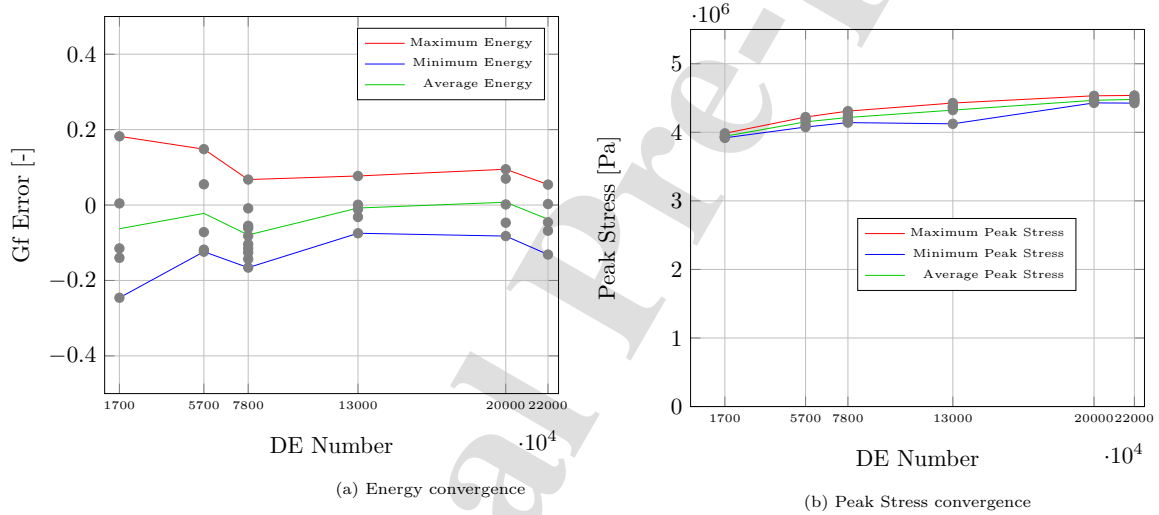
Figure 11: Study of the convergence on a cylinder under tension

Since many of the benefits of the damaging beam model have been discussed,
it would be relevant to focus on the choice of model parameters and their in-
fluence. Thus, the influence of the mixed parameter α on the tensile behavior
500   is studied. Figure 12 represents the results for three different values of α. No
significant variation is detected. The tensile behavior is independent of the α
variable. Thus, as expected, the fracture is purely activated in mode I of fracture
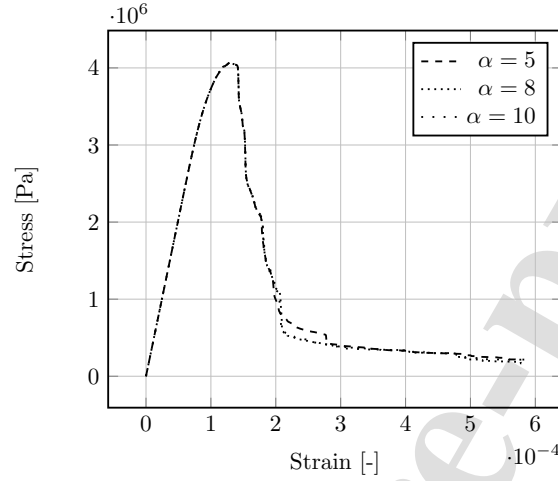of the beams.

30

Figure 12: Stress-stain curve for tensile test with three different α values

This non-influence of alpha on the tensile test highlights the necessity of a
second test to fully calibrate our model. The second testing needs to activate a
mode of fracture different from a pure mode I. Thus, compressing test, largely
studied experimentally, appears as a natural applicant. Another loading of
interest would be compressing testing but performed after a previous damaging
step induced by tensile test. Indeed, such a loading allows emphasizing the
unilateral behavior of concrete.

3.3. Compression Tests

First, an interrupted tensile test followed by a compressing test is carried
out on the cylindrical specimen. When no closure model is used for the simula-
tion, the stiffness in the compressing reloading is equal to the stiffness observed
during the unloading phase of the tensile test. Therefore, no unilateral effect
can be displayed without a closure model. The results for three different meshes
using our closure model are illustrated in the figure 13. As for the convergence
studied for the damaging behavior, a small number of discrete elements seems
to ensure the accuracy of unilateral behavior. Indeed, for a sample composed

31

⁵²⁰ of 5700 elements, unilateral behavior is displayed. Similar results are obtained for coarse and finer meshes as long as the number of elements in the sample is sufficient to model the elastic behavior. Our closure model is convenient and validated for unilateral behavior. However, due to the fact that frictional behavior is not activated in the model, this one fails to describe the value of the
⁵²⁵ residual displacement at zero stress observed from experimental tests or simulated from other discrete element models considering frictional phenomena [66], [67]. Nevertheless, even if the friction phenomenon plays a major role for the quasi-brittle failure especially under compression loading and it is not taken into account in the present model, we choose to simulate a compression test in order
⁵³⁰ to evaluate the capability of the alone damaging beam lattice model under this kind of loading and because compression test involves shear failure required to calibrate the pseudo mode II parameters of the model.
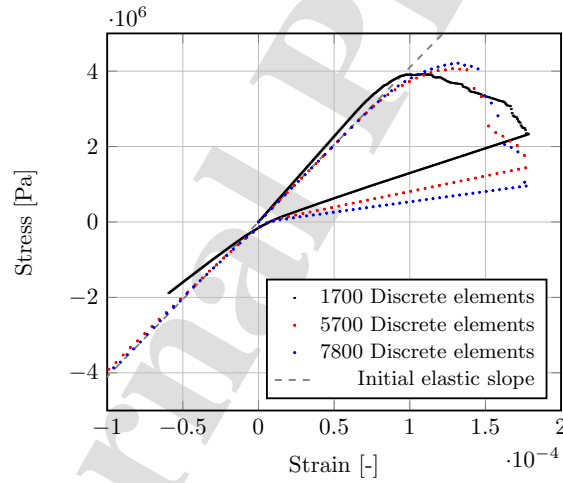

Figure 13: Stress-Strain curve for tensile-compressing tests

Compression tests are undertaken on the cylindrical specimen applying different boundary conditions, illustrated in the figure 14. The interest in sim-
⁵³⁵ ulating these two compression tests lies in obtaining two cracking profiles due

32

to the influence of the boundary conditions on them. Indeed, for a test with frictionless plates, multiple cracks parallel to the loading direction through the specimen are expected. For the test with embedded plates, shear bands should appear within the specimen.

Figure 14: Boundary conditions applied during the friction-less compression test (on the left) and the clamped compression test (on the right)

First, a compressing test is carried out in applying a y-displacement at extremities cross-section while x and z displacements are left free. The parameters of damage evolution remain identical for compressing and tensile tests.

For such boundary conditions, a fracture of the plans parallel to the loading is expected. Figure 15 shows the evolution of the damage field with a top view of the cylinder. Numerous damaged beams are distinguishable through the cylinder. Finally, multiple through-breaks of the cylinder appear in the cylinder, as expected. Nevertheless, damage does not localize in planes parallel to the compressive loading direction. Such a localization undoubtedly requires introducing some noise into the system as internal stresses which will be the object of a future study.

33

(a) t=0.0798 s

(b) t=0.1236 s

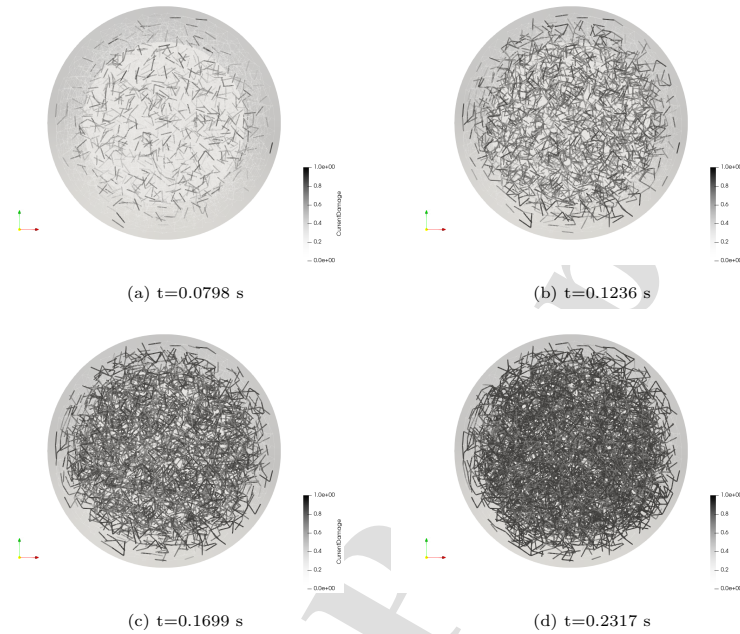(c) t=0.1699 s

(d) t=0.2317 s

Figure 15: Evolution of damage fields during a compressing test with free extremities

Concerning the stress-strain curve presented in figure 16, the behavior of the specimen displays a smoother softening than in tension. In addition, the peak stress is 43 MPa. The compressing and tensile strength ratio is then approximately 10, as observed experimentally [38],[61],[68]. This first compressing test-

555 ing is accurately simulated in terms of global mechanical behavior but leads to diffuse damage compared to the experimental one observed for concrete. To test our model, particularly the crack path prediction, second compressing testing is carried out where a y-displacement is still applied but x and z displacements are blocked to simulate the frictional effect acting on the area of the boundary

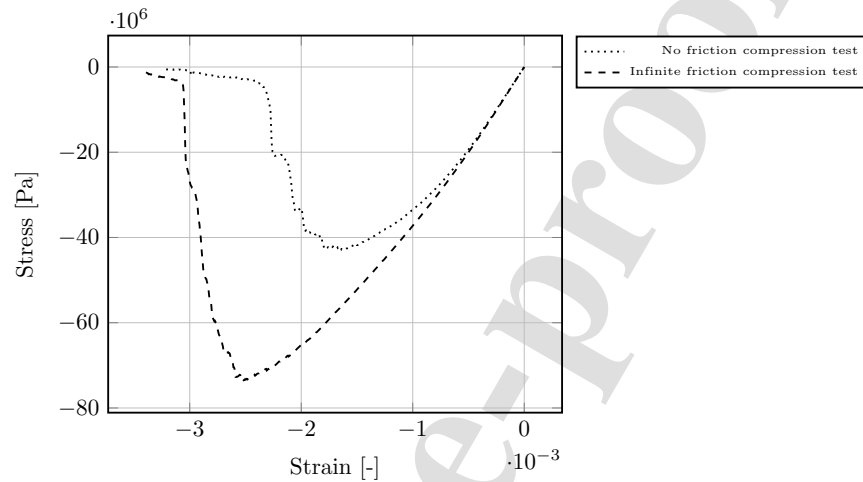560 cross-sections frequently observed during experimental tests.

34

Figure 16: Stress-strain response for compression tests with no friction and infinite friction at the plates.

From a mechanical behavior point of view, a similar stress-strain curve is obtained. A higher stress peak is displayed which is consistent with the larger surface of fracture happening in the specimen. In addition, the evolution of the damage field, illustrated in figure 17, reveals that damaged beams, represented in black in the figure, are more numerous than for the previous compressing test. In order to observe the cracking path, the final damage field where the beams are fully damaged, i.e. for which D=1, is presented in Figure 18. For the sake of clarity, a slice of the specimen is made in order to analyse the cracking profile in one slice of the specimen. Damage is activated in many beams, including those located in cones, due to the embedded end conditions inducing high loading in the specimen, especially in the material volume of the cones. However, a location of the heavily damaged beams as well as the cracking zone is noticeable along the conical surface, as experimentally. This type of break is provided by experimental testing due to the frictional effects between the sample and the plates of the device [69],[70]. Consequently, our model is predictive for the perfect compressive tests, with no frictional effect, and for endless frictional
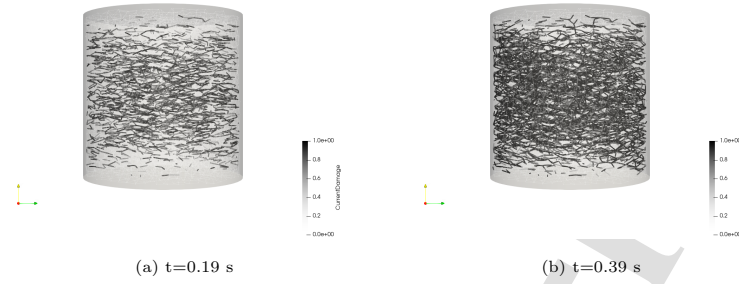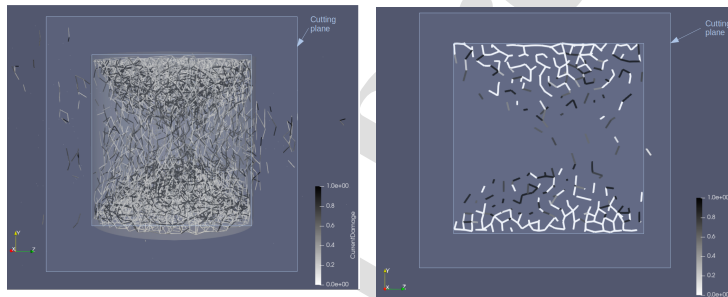
35

effects.

(a) t=0.19 s   (b) t=0.39 s

Figure 17: Evolution of damage fields during a compressing test with clamped extremities

(a) Damage field at the end of a compressing (b) View of the final damage field in a slice
test with clamped extremities where the fully of the specimen
damaged beam ($D = 1$) are removed

Figure 18: Final damage field for a specimen under a compressing test with clamped extremities and its view in a slice of the specimen

In the aim of highlighting the mixed-mode impact during compressing testing, the influence of the α parameter is investigated. In comparison with the
580 tensile test, the fluctuations due to α value are highly apparent. For small values, the contributions of mode I* and mode II* will be of the same amount and the fracture would happen sharply. On the other hand, for a higher α value, larger displacement of mode II* will be needed to fracture. Thus, the use of a high value of α allows to retain a predominant mode I* fracture while dissipating

36

energy in a mode II*. Indeed, without this dissipating in mode II*, i. e. pure mode I*, compressing behavior is not restored. As shown in the figure 19, pure mode I* is not able to display a softening, a higher amount of energy would be necessary for fracture. For a $\alpha = 8$, the curve stress-strain is similar to those obtained from experimental works in the literature, and this in terms of peak stress as well as of the softening part of the stress-strain response.
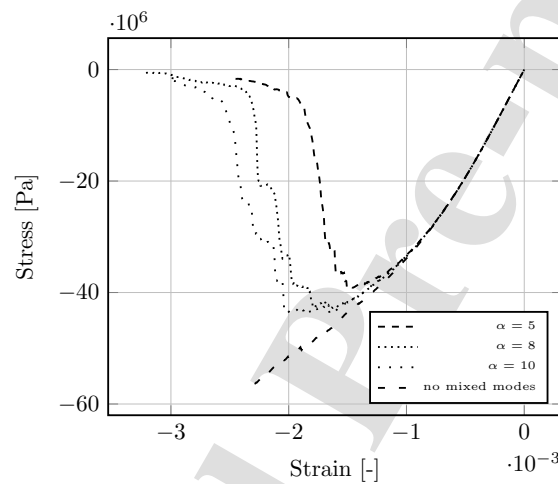

Figure 19: Influence of α value on frictionless compressing stress-strain curve

Let us remember that friction between discrete elements is not activated in the mode while frictional dissipation is well known to be a dominant character of the quasi-brittle failure [50], [51]. As a consequence, taking friction into account in a future version of the model should lead to consider a decrease of the value of the pseudo mode II fracture energy G_{fII*} and/or of the parameter α because a large amount of energy should be dissipated through friction under compression loading. Thus, even if the fracture parameters of pseudo mode II are certainly overestimated due to the absence of friction, the three parameters of our model are determined from compression and tensile tests and the model can be used for simulation of experimental tests in which most of the cracking is induced in

37

mixed-mode I+II.

4. Confrontation to experimental mixed-mode cracking : Benchmark Carpiuc

In this section, the model is confronted with experimental work. For this purpose, particular attention is directed to two trials carried out in the framework of the *Carpiuc* benchmark [71] where data are available in the Zenodo website [72]. This benchmark is an ideal candidate for testing our model due to its focus on the complex mixed-mode loading of mortar specimens. For these tests, a hexapod machine is used to apply complex loading. Indeed, the 6-axis testing machine, illustrated in figure 20 allows to apply up to 3 forces and 3 moments simultaneously. The specimen is inserted between two plates subjected to these loads to better control the boundary conditions.
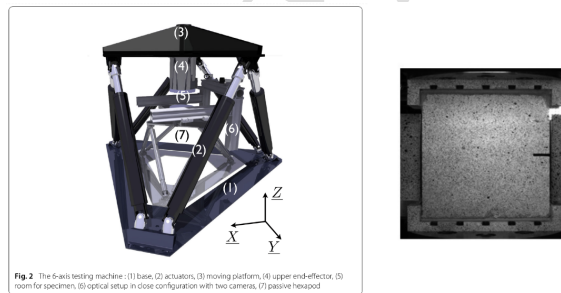

Figure 20: Experimental set-up developped for the Carpiuc benchmark [71]

For both tests simulated here, the applied loading can be split into three components: tension, shear, and bending, as shown in Figure 21.
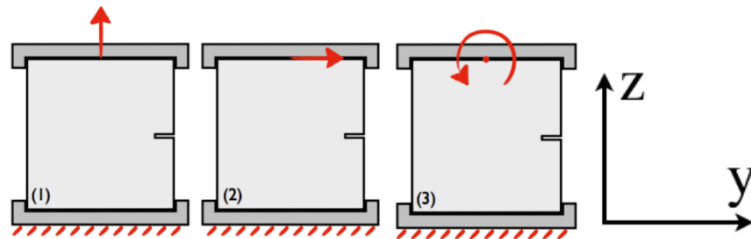
Figure 21: The three elementary loading applied during the tests: tension, shear and torsion [71]

⁶¹⁵ A digital image correlation (DIC) is performed to measure the displacements of the ends of the loaded specimens. As a result, the displacements along Y and Z on the upper and lower faces of the specimen are obtained.

The first test is performed on a single notch specimen. The second test is carried out on a double-notch specimen.

⁶²⁰ Both samples made with 7800 discrete elements are presented in figure 22. Note that the machine setup is such as the specimens are located between two plates on which the displacements are applied. Consequently, the problem is modeled in 2 dimensions.
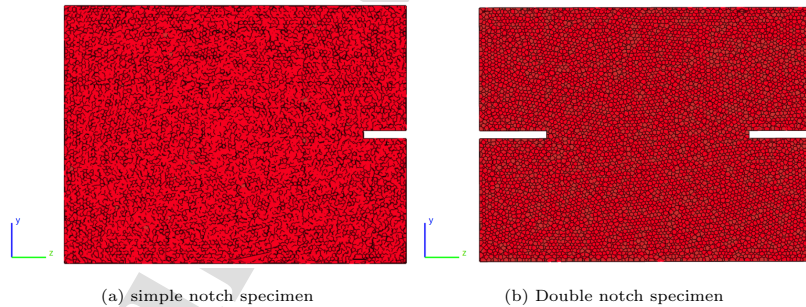

(a) simple notch specimen   (b) Double notch specimen

Figure 22: 2D Voronoi Specimens used for the simulation of the benchmark tests

To simulate these tests, the first step is to determine the Y and Z displace-
⁶²⁵ ments for each discrete element on the top and bottom sides of the specimen.

39

Indeed, the positions of the randomly generated discrete elements do not coincide with those of the DIC measurements. Thus, an interpolation from experimental data is then performed. In a second stage, a calibration of the elastic and damage parameters is undertaken based on the experimental values of the mortar. The input parameters of the simulations are given in table 5.

E_M	17.25 GPa
E_μ	82.97 GPa
$G_{f,\mathrm{I}}$	114.6 $J.m^{-2}$
$\varepsilon_{e,\mathrm{I}}$	2.2 $\times 10^{-4}$
α	8

Table 5: Elastic and Damaging law parameters for the benchmark mortar

To avoid specimen damage near the lower and upper zones of loading application, a correction factor is applied to the damage variables. In fact, the corrective factor F_D follows a top hat law. As shown in figure 23 for a single notched specimen, the corrective factor varies between 0 at the edges of the specimen and 1 in the core of the specimen and thus allows the damage on the edges of the specimen to be canceled out without modifying the damage values on the central part of the specimen.
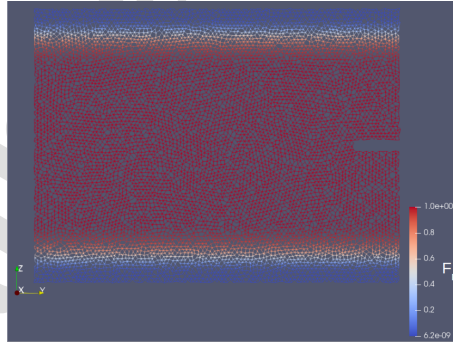

Figure 23: Evolution of the corrective factor F_D value within a single notched specimen

In addition, due to the geometry of the notch and to prevent any influence of the position of the initiation zone along with the notch, the characteristics

₆₄₀ of the beams located at the upper corner of the notch were degraded for the single notch specimen. Indeed, the value of the parameter ε_{I*}^e was decreased to 1.32×10^{-4} allowing early damage in this area. Thus, the crack initiation occurs as experimentally and the abilities of the model to reproduce the crack propagation path can be observed. Similarly, for the double notch specimen,

₆₄₅ the beams in the lower corner of the left notch and the upper corner of the right notch had their maximum elastic deformation reduced.

For each test, the simulation is performed on five different samples.

The tensile and shear forces obtained at the ends of the specimen during the simulation of the five specimens are compared with the forces measured by the

₆₅₀ experimental setup in Figure 24.

(a) Evolution of the tensile force F_z during the single notch test

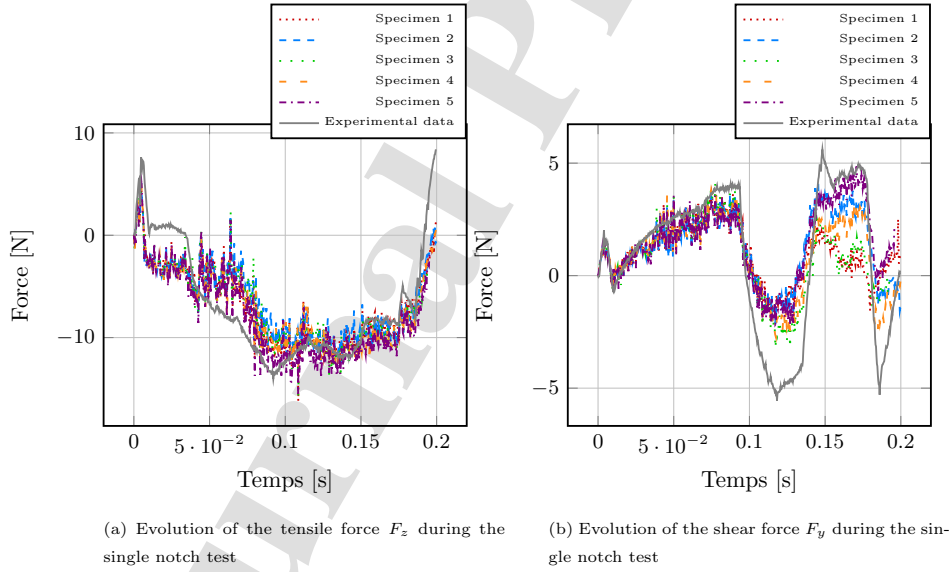(b) Evolution of the shear force F_y during the single notch test

Figure 24: Comparison of the tensile and shear forces obtained from the simulation of five single-notch specimens with those from experiments

41

. Firstly, during the simulation, the forces are measured at the extremities of the digital specimen corresponding to the area where the image correlation is performed. However, the experimental force values are measured at the hexapod level. Thus, due to these differences in the force measurement areas, and the use of image correlation data, noise in the numerical results are noticeable. At the beginning of the test, for a time of less than 0.1 s, the experimentally and numerically measured forces are similar. The only difference lies in the peak force in tension. Indeed, due to the use of specimens composed of 8,000 discrete elements, it has been shown previously that convergence at the peak stress level was not achieved. As a result, an underestimation of the peak force at crack initiation is observed numerically. Concerning the shear force, the experimental and numerical results are confounded for times lower than 0.1 s, i.e. during the crack initiation phase. During the crack bifurcation and branching phases, *i. e.* for times greater than 0.1 s, differences are observed in the experimentally and numerically measured shear forces. These differences can be explained, on the one hand, by the dependence of the experimental results on the mesostructure of the specimen tested and, on the other hand, by the dependence of the value of the shear force measured on the beam network. Indeed, for two specimens such as specimen 1 and specimen 5, the observed shear force varies by a factor of 2. Due to these variations in forces between the different beam arrays, the forces obtained by the test simulation are considered to be representative of the experimental forces.

. With regard to cracking paths, the experimental and numerical results obtained for a single notch specimen are overlapped in the figure 25. The experimental results are shown in the figure with the vertical displacement field changing from yellow to red. In particular, the presence of cracks is experimentally noticed at discontinuities in this displacement field. The damage field obtained with the simulation is presented through the damaged beams, in black. The undamaged beams are transparent so as not to interfere with the analysis of the results.

42

(a) t= 0.0769 s

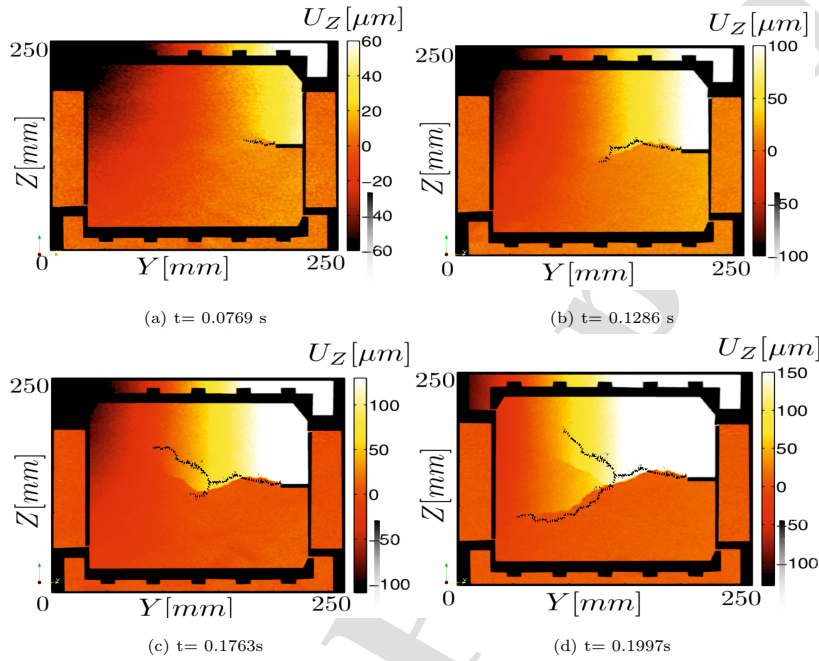(b) t= 0.1286 s

(c) t= 0.1763s

(d) t= 0.1997s

Figure 25: Evolution of damage fields during the mixed-mode test on a single notched specimen (only damage beams are represented in black)

During the first phase, a crack is initiated at the notch, illustrated in figure 25a. Then a change in shear loading induces a reorientation of the crack propagation both experimentally and numerically, displayed in figure 25b. Afterward, a second bifurcation is triggered by a further change in shear loads. Finally, as expected, the imposed loading leads to the successive formation of two distinct cracks, called branches, shown in figures 25c and 25d. These different stages are observed for each of the five simulated specimens. This test highlights the ability of the model to predict crack bifurcation as well as its robustness to sudden changes in loading. The mechanisms of crack closure and crack coalescence are studied thanks to the simulation of the second test. Firstly, the evolution of the tensile and shear forces at the ends is studied and presented in figure 26.

43
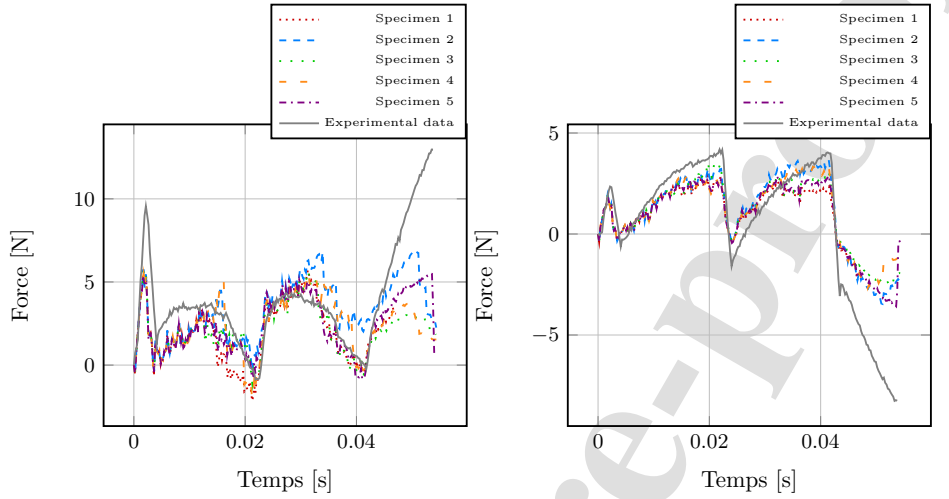
(a) Evolution of the tensile force F_z during the double notch test

(b) Evolution of the shear force F_y during the double notch test

Figure 26: Comparison of the tensile and shear forces obtained from the simulation of five double-notch specimens with those from experiments

. As with the single notch test, the crack initiation and propagation phases are not dependent on the initial beam network. Indeed, the simulated tensile and shear forces are representative of the experimental forces. The peak tensile

695 force is underestimated due to the use of 8,000 element specimens. This test highlights the sensitivity of the crack coalescence phase to the beam network. Indeed, for times greater than 0.1 s, a difference between the five numerical results and the experimental result is notable. The observation of the tensile and shear forces shows that the double notch test is faithfully reproduced, although

700 the crack coalescence at the end of the simulation is dependent on the initial beam network. However, the experimental result studied here corresponds to a specimen with a particular mesostructure. For a specimen with a different mesostructure, the evolution of the tensile and shear forces would not be identical to that presented here. Thus, due to these experimental and numerical

705 variations of the tensile and shear forces, it can be assumed that the model

44

provides a reasonable representation of the forces within the specimen. The damage field obtained for three times of the simulation is shown and compared to the experimental crack path in figure 27.
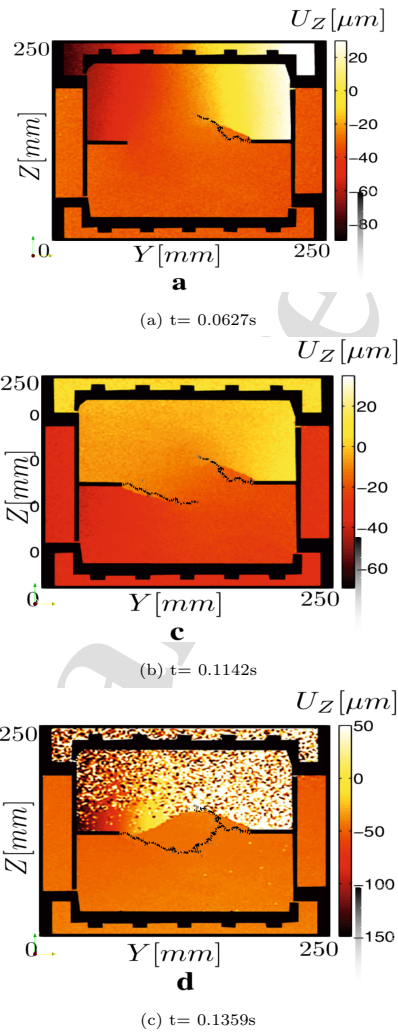

(a) t= 0.0627s

(b) t= 0.1142s

(c) t= 0.1359s

Figure 27: Evolution of damage fields during the mixed-mode test on a double notched specimen (only damage beams are represented in black)

45

As experimentally, a first crack is initiated at the right notch, observed in
710   figure 27a. In a second stage, the specimen is unloaded to close the crack. A
new loading is then applied to the specimen to initiate a second crack without
propagation of the first crack. The initiation of the second crack is displayed
in figure 27b. In the final step, the loading is increased dramatically to reopen
the two cracks and allow them to reorient and coalesce. This coalescence mech-
715   anism is highly unstable. The simulation results show a coalescence due to the
propagation of the second crack in contrast to the experimental results where
the first crack propagates, illustrated in figure 27c. There are many reasons for
these differences. First, the initiation part of the test has a great impact on the
crack path. In addition, in this experimental work, a pre-cycle of elastic loading
720   and unloading is applied to the specimen inducing a locally pre-stressed state,
different for each specimen tested. In addition, the mortar mesostructure influ-
ences the location of crack initiation. These pre-stress and mesostructure effects
are not taken into account in the model and explain the differences observed
during the unsteady propagation phase.

725   **5. Conclusion and Perspectives**

A new damage beam-lattice model inspired by cohesive zone models has
been presented. If this model is dedicated to discrete element modeling, it is
implemented in this first version without resorting to the friction modeling in
order to study the alone capabilities of the damage beam-lattice to describe
730   quasi-brittle cracking mostly induced in mixed mode I+II. Only the contact de-
tection between neighboring discrete elements is activated in order to describe
unilateral behavior. The main advantage of this model is the reduced number
of parameters which can be easily determined from two experimental tests, one
tensile and one compression test. Five qualitative tests have been performed
735   on concrete-like specimens. Among these tests, only two, monotonic tensile and
compressive tests are required to calibrate the damaging beam model. A second
compressing test has been used to verify that the set of calibrated parameters

46

is suitable and in accordance with the classical shape of mechanical response of quasi-brittle materials. The peak stresses and cracking paths expected are displayed. In particular, the compressing and tensile peak stress ratio is estimated at 10 which is the typical value observed for concrete. Nevertheless, comparisons with data from experimental tests need to be performed to finally validated either the calibration protocol and the prediction capability of the proposed approach. In addition, it has been shown that a microscopic damaging behavior induces a macroscopic damaging behavior. The methodology of energy calibration which has been presented allows displaying macroscopically energy dissipated equally to the cohesive energy input. Furthermore, it has demonstrated that convergence appears for specimens with few elements. The elasticity convergence, reached for approximately 5 000 discrete elements, ensures a good accuracy of the damaging behavior. Thus, the damaging beam model could be a good candidate for structure simulation.

The mechanism of crack reclosure has also been studied. The interrupted tensile test with a release followed by a compressing test has shown that the contact model developed allows taking into account the unilateral behavior of the material. However, as expected due to the fact that frictional behavior between discrete elements is deactivated, the model fails to describe the value of residual displacement at zero stress observed from experiments or simulated by other discrete models in the litterature that already take into account the coulomb law for friction. Special interest should be focused on these frictional aspects during further work. Indeed, better modeling of the frictional contribution could result in a larger residual displacement and hysteresis effects. The improvement of the present model is being developed to introduce friction effects as well as internal stresses within the lattice. This will be tested using a tension-compression test [61], which is more suitable for studying the dissipative mechanisms involved in crack reclosure.

Finally, the model was compared with the experimental results of the Carpiuc benchmark in which cracking is mostly induced in mixed mode I+II. Tests with complex mixed-mode loading on single and double notched specimens high-

47

lighted the ability of our model to predict bifurcation and crack branching phe-
nomena. Indeed, for each of the tests, the cracking paths predicted by the
model are consistent with those observed experimentally. An improvement of
the model could be achieved at the level of crack initiation, in particular by
taking into account the pre-stressed states present within the material and the
mesostructure of mortars and concretes.

References

References

[1] T. Belytschko, T. Black, Elastic crack growth in finite elements with mini-
mal remeshing, International Journal for Numerical Methods in Engineer-
ing 45 (5) (1999) 601–620.

[2] N. Moës, J. Dolbow, T. Belytschko, A finite element method for crack
growth without remeshing, International Journal for Numerical Methods
in Engineering 46 (1) (1999) 131–150.

[3] N. Moës, T. Belytschko, X-fem, de nouvelles frontières pour les éléments
finis.

[4] F. Ragueneau, C. L. Borderie, J. Mazars, Damage model for concrete-like
materials coupling cracking and friction, contribution towards structural
damping: first uniaxial applications, Mechanics of Cohesive-Frictional Ma-
terials.

[5] Z. P. Bazant, L. Cedolin, Finite element modeling of crack band prop-
agation, Journal of Structural Engineering 109 (1) (1983) 69–92. doi:
10.1061/(ASCE)0733-9445(1983)109:1(69).

[6] J. Mazars, Y. Berthaud, S. Ramtani, The unilateral behaviour of damaged
concrete, Engineering Fracture Mechanics.

48

[7] S. Fichant, C. La Borderie, G. Pijaudier-Cabot, Isotropic and anisotropic descriptions of damage in concrete structures, Mechanics of Cohesive-frictional Materials 4 (4) (1999) 339–359.

[8] G. Pijaudier-Cabot, Z. Bazant, Nonlocal damage theory, Journal of Engineering Mechanics-asce - J ENG MECH-ASCE 113. doi:10.1061/(ASCE) 0733-9399(1987)113:10(1512).

[9] M. Frémond, B. Nedjar, Damage, gradient of damage and principle of virtual power, International Journal of Solids and Structures 33 (1996) 1083–1103. doi:10.1016/0020-7683(95)00074-7.

[10] M. van den Bosch, P. Schreurs, M. Geers, An improved description of the exponential xu and needleman cohesive zone law for mixed-mode decohesion, Engineering Fracture Mechanics 73 (9) (2006) 1220–1234. doi:https://doi.org/10.1016/j.engfracmech.2005.12.006.

[11] N. Dourado, S. Morel, M. De Moura, G. Valentin, J. Morais, Comparison of fracture properties of two wood species through cohesive crack simulations, Composites Part A-applied Science and Manufacturing - COMPOS PART A-APPL SCI MANUF 39 (2008) 415–427. doi:10.1016/j.compositesa. 2007.08.025.

[12] G. Camacho, M. Ortiz, Computational modelling of impact damage in brittle materials, International Journal of Solids and Structures 33 (20) (1996) 2899–2938. doi:https://doi.org/10.1016/0020-7683(95)00255-3.

[13] G. Francfort, J.-J. Marigo, Revisiting brittle fracture as an energy minimization problem, Journal of the Mechanics and Physics of Solids 46 (8) (1998) 1319–1342. doi:https://doi.org/10.1016/S0022-5096(98) 00034-9.
URL https://www.sciencedirect.com/science/article/pii/ S0022509698000349

49

[14] C. Miehe, F. Welschinger, M. Hofacker, Thermodynamically consistent phase-field models of fracture: Variational principles and multi-field fe implementations, International Journal for Numerical Methods in Engineering 83 (10) (2010) 1273–1311. `arXiv:https://onlinelibrary.wiley.com/doi/pdf/10.1002/nme.2861`, `doi:https://doi.org/10.1002/nme.2861`.
URL `https://onlinelibrary.wiley.com/doi/abs/10.1002/nme.2861`

[15] M. J. Borden, C. V. Verhoosel, M. A. Scott, T. J. Hughes, C. M. Landis, A phase-field description of dynamic brittle fracture, Computer Methods in Applied Mechanics and Engineering 217-220 (2012) 77–95. `doi:https://doi.org/10.1016/j.cma.2012.01.008`.
URL `https://www.sciencedirect.com/science/article/pii/S0045782512000199`

[16] T. Nguyen, J. Yvonnet, Q.-Z. Zhu, M. Bornert, C. Chateau, A phase field method to simulate crack nucleation and propagation in strongly heterogeneous materials from direct imaging of their microstructure, Engineering Fracture Mechanics 139 (2015) 18–39. `doi:https://doi.org/10.1016/j.engfracmech.2015.03.045`.
URL `https://www.sciencedirect.com/science/article/pii/S0013794415001332`

[17] H. J. Herrmann, S. Roux, 5 - modelization of fracture in disordered systems, in: H. J. Herrmann, S. Roux (Eds.), Statistical Models for the Fracture of Disordered Media, Random Materials and Processes, North-Holland, Amsterdam, 1990, pp. 159–188. `doi:https://doi.org/10.1016/B978-0-444-88551-7.50016-1`.

[18] H. A. Carmona, F. K. Wittel, F. Kun, From fracture to fragmentation: Discrete element modeling, The European Physical Journal Special Topics 223 (11) (2014) 2369–2382. `doi:10.1140/epjst/e2014-02270-3`.

[19] D. André, M. Jebahi, I. Iordanoff, J. luc Charles, J. Néauport, Using the discrete element method to simulate brittle fracture in the indentation of a

50

850 silica glass with a blunt indenter, Computer Methods in Applied Mechanics
and Engineering 265 (2013) 136–147. `doi:https://doi.org/10.1016/j.cma.2013.06.008.`

[20] E. Schlangen, E. Garboczi, New method for simulating fracture
using an elastically uniform random geometry lattice, Interna-
855 tional Journal of Engineering Science 34 (10) (1996) 1131–1144.
`doi:https://doi.org/10.1016/0020-7225(96)00019-5.`
URL `https://www.sciencedirect.com/science/article/pii/0020722596000195`

[21] B. Šavija, M. Luković, J. Pacheco, E. Schlangen, Cracking of the con-
860 crete cover due to reinforcement corrosion: A two-dimensional lattice
model study, Construction and Building Materials 44 (2013) 626–638.
`doi:https://doi.org/10.1016/j.conbuildmat.2013.03.063.`
URL `https://www.sciencedirect.com/science/article/pii/S0950061813002730`

865 [22] I. Iordanoff, A. Battentier, J. Néauport, J. Charles, A discrete element
model to investigate sub-surface damage due to surface polishing, Tribology
International 41 (11) (2008) 957–964, tribological Contacts and Component
Life: Proceedings of the 34th Leeds-Lyon Symposium on Tribology. `doi:https://doi.org/10.1016/j.triboint.2008.02.018.`

870 [23] B. Schneider, M. Bischoff, E. Ramm, Modeling of material failure by the
discrete element method, PAMM 10 (1) (2010) 685–688. `doi:https://doi.org/10.1002/pamm.201010329.`

[24] Mariotti, C., Michaut, V., Molinari, J. F., Modeling of the fragmentation
by discrete element method, DYMAT - International Conference on the
875 Mechanical and Physical Behaviour of Materials under Dynamic Loading
2 (2009) 1523–1528. `doi:10.1051/dymat/2009215.`

[25] F. A. Tavarez, M. E. Plesha, Discrete element method for modelling solid
and particulate materials, International Journal for Numerical Methods in

51

Engineering 70 (4) (2007) 379–404. doi:https://doi.org/10.1002/nme.880   1881.

[26] G. Cusatis, Z. P. Bažant, L. Cedolin, Confinement-shear lattice model for concrete damage in tension and compression: I. theory, Journal of Engineering Mechanics 129 (12) (2003) 1439–1448. doi:10.1061/(ASCE)0733-9399(2003)129:12(1439).

885 [27] G. Cusatis, Z. P. Bažant, L. Cedolin, Confinement-shear lattice csl model for fracture propagation in concrete, Computer Methods in Applied Mechanics and Engineering 195 (52) (2006) 7154–7171, computational Modelling of Concrete. doi:https://doi.org/10.1016/j.cma.2005.04.019. URL   https://www.sciencedirect.com/science/article/pii/890   S0045782505003956

[28] T. Kawai, New discrete models and their application to seismic response analysis of structures, Nuclear Engineering and Design 48 (1) (1978) 207–229, special Issue Structural Mechanics in Reactor Technology - Smirt-4. doi:https://doi.org/10.1016/0029-5493(78)90217-0.
895   URL   https://www.sciencedirect.com/science/article/pii/0029549378902170

[29] J. E. Bolander, N. Sukumar, Irregular lattice model for quasistatic crack propagation, Phys. Rev. B 71 (2005) 094106. doi:10.1103/PhysRevB.71.094106.
900   URL https://link.aps.org/doi/10.1103/PhysRevB.71.094106

[30] C. O. Oliver-Leblond, Beam-particle approach to model the quasi-brittle behaviour of concrete CARPIUC Benchmark, in: Fifth International Conference on Computational Modeling of Fracture and Failure of Materials and Structures (CFRAC2017), Nantes, France, 2017.

905 [31] W. Leclerc, H. Haddad, M. Guessasma, On a discrete element method to simulate thermal-induced damage in 2d composite materials, Comput-

ers Structures 196 (2018) 277–291. doi:https://doi.org/10.1016/j.
compstruc.2017.10.008.

[32] E. Schlangen, E. Garboczi, Fracture simulations of concrete using lat-
tice models: Computational aspects, Engineering Fracture Mechanics
57 (2) (1997) 319–332. doi:https://doi.org/10.1016/S0013-7944(97)
00010-6.

[33] X. Gao, G. Koval, C. Chazallon, A discrete element model for damage
and fatigue crack growth of quasi-brittle materials, Advances in Materials
Science and Engineering 2019 (2019) 1–15. doi:10.1155/2019/6962394.

[34] Y.-L. Gui, H. H. Bui, J. Kodikara, Q.-B. Zhang, J. Zhao, T. Rabczuk,
Modelling the dynamic failure of brittle rocks using a hybrid continuum-
discrete element method with a mixed-mode cohesive fracture model, In-
ternational Journal of Impact Engineering 87 (2016) 146–155, sI: Ex-
perimental Testing and Computational Modeling of Dynamic Fracture.
doi:https://doi.org/10.1016/j.ijimpeng.2015.04.010.

[35] N. H. Nguyen, H. H. Bui, G. D. Nguyen, J. Kodikara, A cohesive damage-
plasticity model for dem and its application for numerical investigation of
soft rock fracture properties, International Journal of Plasticity 98 (2017)
175–196. doi:https://doi.org/10.1016/j.ijplas.2017.07.008.

[36] A. Hillerborg, M. Modéer, P.-E. Petersson, Analysis of crack formation
and crack growth in concrete by means of fracture mechanics and finite
elements, Cement and Concrete Research 6 (6) (1976) 773–781. doi:https:
//doi.org/10.1016/0008-8846(76)90007-7.

[37] T. Vandellos, E. Martin, D. Leguillon, Comparison between cohesive zone
models and a coupled criterion for prediction of edge debonding, in: 16th
European Conference on Composite Materials, SEVILLE, Spain, 2014.
URL https://hal-onera.archives-ouvertes.fr/hal-01069269

[38] L. Snozzi, F. Gatuingt, J.-F. Molinari, A meso-mechanical model for con-
crete under dynamic tensile and compressive loading, International Journal
of Fracture 178 (2012) 179–194. doi:10.1007/s10704-012-9778-z.

[39] P.-E. Petersson, Crack growth and development of fracture zones in plain
concrete and similar materials, Ph.D. thesis, Lund University (1981).

[40] A. Phan, M. Chaplain, S. Morel, J.-L. Coureau, Influence of moisture
content on mode i fracture process of pinus pinaster: evolution of micro-
cracking and crack-bridging energies highlighted by bilinear softening in
cohesive zone model, Wood Science and Technology 51 (2017) 1051–1066.
doi:10.1007/s00226-017-0907-8.

[41] K. Park, G. H. Paulino, J. Roesler, Cohesive fracture model for functionally
graded fiber reinforced concrete, Cement and Concrete Research 40 (6)
(2010) 956–965. doi:https://doi.org/10.1016/j.cemconres.2010.02.
004.

[42] F. Evangelista, J. R. Roesler, S. P. Proença, Three-dimensional cohesive
zone model for fracture of cementitious materials based on the thermody-
namics of irreversible processes, Engineering Fracture Mechanics 97 (2013)
261–280. doi:https://doi.org/10.1016/j.engfracmech.2012.10.023.

[43] X. Xu, A. Needleman, Void nucleation by inclusion debonding in a crystal
matrix, Modelling and Simulation in Materials Science and Engineering 1
(1999) 111. doi:10.1088/0965-0393/1/2/001.

[44] G. W. Zhu, Y. X. Jia, P. Qu, J. Q. Nie, Y. L. Guo, Effect of characteristic
parameters of exponential cohesive zone model on mode i fracture of lam-
inated composites, in: Advances in Fracture and Damage Mechanics XI,
Vol. 525 of Key Engineering Materials, Trans Tech Publications Ltd, 2013,
pp. 409–412. doi:10.4028/www.scientific.net/KEM.525-526.409.

[45] S. Song, G. Paulino, W. Buttlar, Cohesive zone simulation of mode i and

mixed-mode crack propagation in asphalt concrete, 2005, pp. 1–10. `doi:`
`10.1061/40776(155)15`.

[46] M. J. van den Bosch, P. J. G. Schreurs, M. G. D. Geers, A new cohesive
zone model for mixed-mode decohesion, in: E. E. Gdoutos (Ed.), Fracture
of Nano and Engineering Materials and Structures, Springer Netherlands,
Dordrecht, 2006, pp. 973–974.

[47] V. Venzal, S. Morel, T. Parent, F. Dubois, Frictional cohesive zone model
for quasi-brittle fracture: Mixed-mode and coupling between cohesive
and frictional behaviors, International Journal of Solids and Structures
198 (2020) 17–30. `doi:https://doi.org/10.1016/j.ijsolstr.2020.04.`
`023`.

[48] P. Grassl, M. Jirásek, Meso-scale approach to modelling the fracture process
zone of concrete subjected to uniaxial tension, International Journal of
Solids and Structures 47 (7-8) (2010) 957–968. `arXiv:0901.4636`, `doi:`
`10.1016/j.ijsolstr.2009.12.010`.

[49] P. Grassl, D. Grégoire, L. Rojas Solano, G. Pijaudier-Cabot, Meso-scale
modelling of the size effect on the fracture process zone of concrete, In-
ternational Journal of Solids and Structures 49 (13) (2012) 1818–1827.
`arXiv:1107.2311`, `doi:10.1016/j.ijsolstr.2012.03.023`.

[50] Z. Bažant, Analysis of work-of-fracture method for measuring fracture en-
ergy of concrete, Journal of Engineering Mechanics - ASCE 122 (2) (1996)
138–144. `doi:10.1061/(ASCE)0733-9399(1996)122:2(138)`.

[51] E. N. Landis, E. N. Nagy, D. T. Keane, Microstructure and fracture in
three dimensions, Engineering Fracture Mechanics 70 (7) (2003) 911–925.
`doi:https://doi.org/10.1016/S0013-7944(02)00157-1`.
URL `https://www.sciencedirect.com/science/article/pii/`
`S0013794402001571`

[52] L. Hedjazi, C. Martin, S. Guessasma, G. Della Valle, R. Dendievel, Application of the discrete element method to crack propagation and crack branching in a vitreous dense biopolymer material, International Journal of Solids and Structures 49 (13) (2012) 1893–1899. doi:https://doi.org/10.1016/j.ijsolstr.2012.03.030.
URL https://www.sciencedirect.com/science/article/pii/S0020768312001321

[53] A. Carpiuc-Prisacari, C. Jailin, M. Poncelet, K. Kazymyrenko, H. Leclerc, F. Hild, Experimental database of mixed-mode crack propagation tests performed on mortar specimens with a hexapod and full-field measurements. part ii: interactive loading, Cement and Concrete Research 125 (2019) 105867. doi:https://doi.org/10.1016/j.cemconres.2019.105867.

[54] D. André, J. luc Charles, I. Iordanoff, J. Néauport, The granoo workbench, a new tool for developing discrete element simulations, and its application to tribological problems, Advances in Engineering Software 74 (2014) 40–48. doi:https://doi.org/10.1016/j.advengsoft.2014.04.003.

[55] D. André, I. Iordanoff, J. luc Charles, J. Néauport, Discrete element method to simulate continuous material by using the cohesive beam model, Computer Methods in Applied Mechanics and Engineering 213-216 (2012) 113–125. doi:https://doi.org/10.1016/j.cma.2011.12.002.

[56] P. P. Camanho, C. G. Davila, M. F. de Moura, Numerical simulation of mixed-mode progressive delamination in composite materials, Journal of Composite Materials 37 (16) (2003) 1415–1438. arXiv:https://doi.org/10.1177/0021998303034505, doi:10.1177/0021998303034505.
URL https://doi.org/10.1177/0021998303034505

[57] D. Grégoire, L. Rojas-Solano, V. Lefort, P. Grassl, G. Pijaudier-Cabot, Size and boundary effects during failure in quasi-brittle materials: Experimental and numerical investigations, Procedia Materials Science 3 (2014) 1269–

1278, 20th European Conference on Fracture. doi:https://doi.org/10.1016/j.mspro.2014.06.206.

[58] C.-C. Vu, J. Weiss, O. Plé, D. Amitrano, D. Vandembroucq, Revisiting statistical size effects on compressive failure of heterogeneous materials, with a special focus on concrete, Journal of the Mechanics and Physics of Solids 121 (2018) 47–70. doi:https://doi.org/10.1016/j.jmps.2018.07.022.

[59] A. Fernández-Canteli, L. Castañón Jano, B. Nieto, M. Lozano García, T. Holušová, S. Seitl, Determining fracture energy parameters of concrete from the modified compact tension test, Vol. 30, 2014. doi:10.3221/IGF-ESIS.30.46.

[60] J. Lee, M. Lopez, An experimental study on fracture energy of plain concrete, International Journal of Concrete Structures and Materials 8 (2014) 129–139. doi:10.1007/s40069-014-0068-1.

[61] O. Nouailletas, C. L. Borderie, C. Perlot, P. Rivard, G. Ballivy, Experimental study of crack closure on heterogeneous quasi-brittle material, Journal of Engineering Mechanics 141 (11) (2015) 04015041. doi:10.1061/(ASCE)EM.1943-7889.0000928.

[62] T. Nguyen, J. Yvonnet, M. Bornert, C. Chateau, Initiation and propagation of complex 3d networks of cracks in heterogeneous quasi-brittle materials: Direct comparison between in situ testing-microct experiments and phase field simulations, Journal of the Mechanics and Physics of Solids 95 (2016) 320–350. doi:https://doi.org/10.1016/j.jmps.2016.06.004.

[63] D. Xenos, D. Grégoire, S. Morel, P. Grassl, Calibration of nonlocal models for tensile fracture in quasi-brittle heterogeneous materials, Journal of the Mechanics and Physics of Solids 82 (2015) 48–60. doi:https://doi.org/10.1016/j.jmps.2015.05.019.

[64] J. Ulfkjaer, L. Hansen, S. Qvist, S. Madsen, Fracture energy of plain concrete beams at different rates of loading, in: International Conference on ₁₀₄₅ Structures Under Shock and Impact, SUSI, Computational Mechanics Inc, 1996, pp. 415–425, proceedings of the 1996 4th International Conference on Structures Under Shock and Impact, SUSI 96 ; Conference date: 01-07-1996 Through 01-07-1996.

[65] D. Grégoire, L. Rojas-Solano, G. Pijaudier-Cabot, Failure and size effect ₁₀₅₀ for notched and unnotched concrete beams, International Journal for Numerical and Analytical Methods in Geomechanics 37 (2013) 1434–1452. doi:10.1002/nag.2180.

[66] S. Sinaie, Application of the discrete element method for the simulation of size effects in concrete samples, International Journal of Solids and Structures 108 (2017) 244–253. doi:https://doi.org/10.1016/j.ijsolstr.2016.12.022.
URL https://www.sciencedirect.com/science/article/pii/S002076831630395X

[67] N. Nguyen, H. Bui, J. Kodikara, A. Southararajah, G. Nguyen, P. Jit- ₁₀₆₀ sangiam, Discrete element modelling of fracture in quasi-brittle materials, 2016, pp. 329–336. doi:10.1201/9781315226460-49.

[68] A. Gangnant, J. Saliba, C. La Borderie, S. Morel, Modeling of the quasibrittle fracture of concrete at meso-scale: Effect of classes of aggregates on global and local behavior, Cement and Concrete Research 89 (2016) 35–44. ₁₀₆₅ doi:https://doi.org/10.1016/j.cemconres.2016.07.010.

[69] T. Simon, A. Borosnyói, M. Márton, The effect of friction on the compressive strength of concrete specimens. in: Balázs l gy, lublóy É pp. 443-446. isbn: 978-963-313-036-0 the proceedings may be downloaded from : http://fib.bme.hu/konyvek.html, 2011, pp. 443–446.

₁₀₇₀ [70] M. A. Caldarone, R. G. Burg, Importance of end surface preparation when testing high strength concrete cylinders, HPC Bridge Views 57 (2009) 9–11.

[71] A. Carpiuc, M. Poncelet, J. Réthoré, S. Roux, CARPIUC benchmark overview: crack advance, reorientation, propagation and initiation under complex loadings, Advanced Modeling and Simulation in Engineering Sciences 5 (1). doi:10.1186/s40323-018-0115-6.

[72] P. Martin, Data for mixed mode fracture test 1 (CARPIUC Benchmark) (Nov. 2018). doi:10.5281/zenodo.1477016.

6. Appendix : curvilinear lenght computation

Curve length determination is the result of mathematical work. Indeed, the curve length is calculated from the space parametrization of the beam. Following the figure 28 presenting the framework for the cylindrical beam, the y and z expressions as functions of x are related to curve length with the equation:

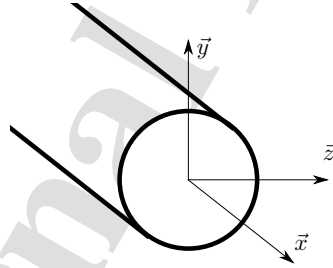$$L_{curve}(t) = \int_0^L \sqrt{1 + y'(x)^2 + z'(x)^2}\, dx \tag{15}$$

Figure 28: Local framework for the beam.

Beam displacements can be defined by a 3rd polynomial function as following:

$$\begin{cases} y(x) &=& A_y x^3 + B_y x^2 + C_y x + D_y \\ z(x) &=& A_z x^3 + B_z x^2 + C_z x + D_z \end{cases} \tag{16}$$

59

To determine the constants of these polynomials, it is necessary to write 4 equations for each position variable y and z. However, the only information known is on discrete element displacements and rotations. In other terms, the y and z positions of extremities $x = 0$ and $x = L$ are given and provide two equations. The two last equations missing are obtained thanks to rotations which are derivative values in $x = 0$ and $x = L$. Taking into account these boundary conditions allows system solving. From the resulting y and z expressions and as well their derivatives, curve length is obtained through numerical integration.

60

Declaration of interests

☒ The authors declare that they have no known competing financial interests or personal relationships that could have appeared to influence the work reported in this paper.

☐The authors declare the following financial interests/personal relationships which may be considered as potential competing interests: